

HYDROGEN EMBRITTLEMENT IN FE-S ALLOYS
(PERMEATION STUDIES)

A Thesis

Submitted to the Graduate Faculty of the
Louisiana State University and
Agricultural and Mechanical College
in partial fulfillment of the
requirements for the degree of
Master of Science

in

The Department of Mechanical Engineering

by
Dale A. Jones
B.S., Louisiana State University, 1980
December, 1981

ACKNOWLEDGMENTS

I would like to express my appreciation to Dr. T. C. Shelton who served as my major professor and first interested me in hydrogen embrittlement. I am particularly grateful for the many hours which he worked with me on this research.

Much appreciation is due Professor W. N. Sharpe, Professor A. J. McPhate, Dr. N. C. Elfer, and Professor F. A. Iddings who served on my examining committee.

Various people in the Mechanical Engineering Department have made valuable contributions to this thesis. In particular, I would like to extend my gratitude to Raymond Gostkowski who singlehandedly built the potentiostat and galvanostat circuits used in all permeation experiments.

Particular mention is due to Mary Duplantis for her encouragement and for typing the many drafts and final copy of this thesis.

2.4

2.5

2.6

2.7

TABLE OF CONTENTS

| | <u>Page</u> |
|---|-------------|
| ACKNOWLEDGMENTS..... | ii |
| LIST OF TABLES..... | vi |
| LIST OF FIGURES..... | vii |
| ABSTRACT..... | ix |
| Chapter 1 INTRODUCTION..... | 1 |
| Chapter 2 THEORY AND LITERATURE REVIEW..... | 4 |
| 2.1 The State of Hydrogen in Metals..... | 4 |
| 2.2 The Forms of Hydrogen in Metals..... | 4 |
| 2.3 Theories of Hydrogen Embrittlement..... | 5 |
| 2.3.1 The Pressure Theory..... | 6 |
| 2.3.2 The Reduction of Cohesive Energy..... | 6 |
| 2.3.3 The Reduction of Surface Free Energy..... | 6 |
| 2.3.4 The Trap Theory..... | 7 |
| 2.4 Diffusion Models..... | 8 |
| 2.4.1 Simple Diffusion Theory..... | 8 |
| 2.4.2 Diffusion Behavior with Trapping..... | 11 |
| 2.5 Characterization of Hydrogen Traps..... | 14 |
| 2.6 The Thermodynamic Force Between Sulfur and Hydrogen..... | 17 |
| 2.7 Hydrogen Embrittlement in Steel Containing Sulfide Inclusions..... | 18 |

TABLE OF CONTENTS (cont.)

| | <u>Page</u> |
|--|-------------|
| Chapter 3 EXPERIMENTAL..... | 21 |
| 3.1 Alloy Preparation..... | 21 |
| 3.1.1 The Phase Diagram of the Fe-S System..... | 21 |
| 3.1.2 Chemical Composition of the Alloys..... | 21 |
| 3.1.3 Melting and Processing the Alloys..... | 23 |
| 3.2 Microstructural Analysis Techniques..... | 27 |
| 3.2.1 Preparation for Microstructural Examination... | 27 |
| 3.2.2 Grain Size..... | 27 |
| 3.2.3 Internal Cracking..... | 28 |
| 3.2.4 Sulfide Inclusions..... | 28 |
| 3.3 Experimental Techniques..... | 29 |
| 3.3.1 The Apparatus..... | 29 |
| 3.3.2 Other Accessories..... | 33 |
| 3.3.3 Setting Up the Experiment..... | 33 |
| Chapter 4 RESULTS AND DISCUSSION..... | 42 |
| 4.1 Microstructural Characterization..... | 42 |
| 4.1.1 Grain Size and Shape..... | 45 |
| 4.1.2 Internal Cracking..... | 45 |
| 4.1.3 Sulfide Inclusions..... | 48 |
| 4.2 Permeation Results..... | 51 |
| 4.2.1 Irreversible Trapping..... | 54 |

TABLE OF CONTENTS (cont.)

| | <u>Page</u> |
|--|-------------|
| 4.2.2 The Possibility of Short-Circuit Diffusion Paths..... | 60 |
| 4.2.3 Surface Effects..... | 61 |
| 4.2.4 Permeation Decay Transients..... | 64 |
| 4.3 Data Analysis..... | 71 |
| 4.3.1 Analysis of Irreversible Trapping..... | 71 |
| 4.3.2 Analysis of Reversible Trapping..... | 78 |
| 4.4 Summary..... | 81 |
| Chapter 5 CONCLUSIONS..... | 82 |
| BIBLIOGRAPHY..... | 83 |
| VITA..... | 86 |

LIST OF TABLES

| | | <u>Page</u> |
|-------------|--|-------------|
| Table I: | Chemical Composition of the Iron Alloys Used in This Study..... | 24 |
| Table II: | Mechanical Processing History of Fe-S Alloys... | 26 |
| Table III: | Oxidation Potentials from Handbook of Chemistry and Physics..... | 34 |
| Table IV: | Grain Size of Each Alloy Calculated by the Lineal Intercept Procedure..... | 46 |
| Table V: | Volume Fraction and Surface Area of Iron-Sulfide Inclusions Found in Each Permeation Membrane..... | 52 |
| Table VI: | Experimental Conditions and Membrane Thickness for Each Permeation Experiment.... | 53 |
| Table VII: | Comparison of First Polarization Apparent Diffusion Coefficient with Values Obtained When Corrected for Relaxation Time..... | 69 |
| Table VIII: | Comparison of Second Polarization Apparent Diffusion Coefficients with Values Obtained When Corrected for Relaxation Time..... | 70 |
| Figure 12: | Flux Normalized to Permeation Area | |
| Figure 13: | Flux Normalized to Permeation Area | |
| Figure 14: | Flux Normalized to Permeation Area | |
| Figure 15: | Effects of First and Second Polarization Transients | |

LIST OF FIGURES

| | <u>Page</u> |
|---|-------------|
| Figure 1: Typical Permeation Transient Showing Experimentally Measured Parameters..... | 10 |
| Figure 2: A Portion of the Iron-Sulfur Phase Diagram..... | 22 |
| Figure 3: Schematic of Experimental Set-Up Used for all Permeations..... | 31 |
| Figure 4: Decay of the Residual Current in the Anode Chamber..... | 40 |
| Figure 5: X-Ray Fluorescence Spectrum of a Ferrite Grain... | 43 |
| Figure 6: X-Ray Fluorescence Spectrum of an Iron-Sulfide Inclusion..... | 44 |
| Figure 7: Representative Micrographs of Fe-S Alloys Showing Grain Structures..... | 47 |
| Figure 8: Representative Micrographs Showing Internal Cracking in Fe-S Alloys..... | 49 |
| Figure 9: Representative Micrographs of FeS Inclusions..... | 50 |
| Figure 10: Flux Normalized First and Second Polarization Permeation Transients for Fe-0.003%S Alloy.... | 55 |
| Figure 11: Flux Normalized First and Second Polarization Permeation Transients for Fe-0.003%S Alloy.... | 56 |
| Figure 12: Flux Normalized First and Second Polarization Permeation Transients for Fe-0.009%S Alloy.... | 57 |
| Figure 13: Flux Normalized First and Second Polarization Permeation Transients for Fe-0.013%S Alloy.... | 58 |
| Figure 14: Flux Normalized First and Second Polarization Permeation Transients for Fe-0.013%S Alloy.... | 59 |
| Figure 15: Effects of Input Surface Contamination on the First and Second Polarization Permeation Transient of an Fe-0.013%S Alloy..... | 63 |

LIST OF FIGURES (contd.)

| | <u>Page</u> |
|---|-------------|
| Figure 16: Normalized Output Flux of Hydrogen Versus Time for the Permeation Decay Transient of Fe-0.003%S Alloy..... | 65 |
| Figure 17: Normalized Output Flux of Hydrogen Versus Time for the Permeation Decay Transient of Fe-0.003%S Alloy..... | 66 |
| Figure 18: Normalized Output Flux of Hydrogen Versus Time for the Permeation Decay Transient of Fe-0.013%S Alloy..... | 67 |
| Figure 19: Normalized Output Flux of Hydrogen Versus Time for the Permeation Decay Transient of Fe-0.013%S Alloy..... | 68 |
| Figure 20: Normalized Permeation Transients for Fe-0.003%S Alloy..... | 72 |
| Figure 21: Normalized Permeation Transients for Fe-0.003%S Alloy..... | 73 |
| Figure 22: Normalized Permeation Transients for Fe-0.013%S Alloy..... | 74 |
| Figure 23: Normalized Permeation Transients for Fe-0.013%S Alloy..... | 75 |
| Figure 24: Quantity of Irreversibly Trapped Hydrogen as a Function of Alloy Sulfur Content..... | 77 |
| Figure 25: Normalized Permeation Rise Transient as Predicted by Simple Diffusion Theory..... | 79 |
| Figure 26: Normalized Permeation Rise Transients for the Second Polarization of Fe-S Alloys Compared With That of Simple Diffusion Theory..... | 80 |

ABSTRACT

The effect of sulfur content on the diffusion and trapping of hydrogen in high purity iron at room temperature has been studied using the electrochemical permeation technique. Polycrystalline iron alloys ranging from Fe-0.003 wt. pct. sulfur to Fe-0.013 wt. pct. sulfur were processed by a series of cold-rolling and annealing steps to obtain fully annealed permeation membranes approximately 1 mm in thickness.

All membranes were charged with hydrogen using a cathodic current density of 0.8 mA/cm^2 . Comparison of the first and second polarization transients of the alloys revealed that iron-sulfide inclusions behave as irreversible hydrogen traps. Also, it was found that neither iron-sulfide inclusions nor solid-solution sulfur in iron behave as reversible hydrogen traps to any measurable degree.

CHAPTER I
INTRODUCTION

The effect of internal hydrogen on metals has been studied by many investigators and the existing literature is voluminous. These investigators have studied the mechanical properties of hydrogen charged metals, the effect of internal hydrogen on the crystal lattice, and the hydrogen diffusion behavior in many types of alloys. Experimental studies also included widely varying microstructures, grain sizes, dislocation densities, alloying elements, phases, and non-metallic inclusions over a wide range of temperatures. Iron and its alloys are the most extensively studied materials with respect to hydrogen embrittlement because, of all the metals, iron is the most susceptible to hydrogen embrittlement. Also, iron alloys are the most widely used engineering materials, and any phenomena which causes the catastrophic and sudden failure of such material should rightfully be the subject of much research.

Permeation measurements have been used for a number of years in an attempt to relate the degradation of the mechanical properties of a metal in the presence of hydrogen to the non-steady state diffusion of hydrogen through the metal. It has been noted that various metallurgical variables such as

grain boundaries [1,2], dislocations [2,3], voids [4,5], substitutional atoms [6], and particle-matrix interfaces [1,2,7] can inhibit the rate of hydrogen diffusion through the metal lattice. Each of these defects in the ideal lattice have a particular interaction energy with hydrogen and are called hydrogen traps.

It is important to identify hydrogen traps because the common denominator of all existing theories of hydrogen embrittlement is that a critical concentration of hydrogen is required at a particular site before hydrogen embrittlement can occur. This indicates that sites of hydrogen trapping may be centers for the nucleation of the hydrogen embrittlement phenomenon. By using the critical concentration concept, Pressouyre [8] has recently defined a set of criteria for the design of alloys which are resistant to hydrogen embrittlement. This involves controlling the microstructure so that it consists of finely and homogeneously distributed irreversible and/or strong reversible hydrogen traps.

Sulfur is a common impurity element found in commercial steels and its detrimental effects on the mechanical properties of steel are well known. In order to reduce the harmful effects of sulfur on steel, manganese is added to the melt where it combines with sulfur to form manganese sulfide. It has recently been shown that manganese sulfide inclusions in steel can behave as nucleation sites for hydrogen cracking [9]. The present research will examine the effect of sulfur content on hydrogen trapping in

high purity iron. Specifically, the effect of iron sulfide inclusions and solid-solution sulfur on the irreversible and reversible trapping characteristics of hydrogen in iron will be examined by the electrochemical permeation technique. This study should provide some insight into the role which sulfur plays in the hydrogen embrittlement of iron base alloys.

(1) a electron) ...
... with elec...
... Also, the ...
... allowing it to move ...
... material. This new ...
... available for physio...

When hydrogen di...
electron to the conduct...
to compensate for its pos...
a strong perturbation [6,11]...
of the metal. Such an atom...
effect of the screened proton...
between neighboring metal atoms

1.1 The Form of Hydrogen in Metals

Once inside the metals, hydrog...
gas at interstitial sites such as cracks...
compounds such as hydrides when combin...
[6], or diffuse through the lattice as

CHAPTER II

THEORY AND LITERATURE REVIEW

2.1 The State of Hydrogen in Metals

Hydrogen is a unique element in that its electronic structure (1 s electron) makes it a highly active element which can easily combine with elements on both the left and right of the periodic table. Also, the atomic size of hydrogen is quite small, allowing it to move relatively rapidly through a crystalline material. This makes hydrogen an element which is readily available for physical and chemical reactions in a metal.

When hydrogen diffuses into a transition metal it loses its electron to the conduction band of the metal [6,10]. In order to compensate for its positive charge, the hydrogen atom induces a strong perturbation [6,11] of electrons in the conduction band of the metal. Such an atom is called a screened proton. The effect of the screened proton, hydrogen, on the binding energy between neighboring metal atoms is not well known.

2.2 The Forms of Hydrogen in Metals

Once inside the metals, hydrogen can form high pressure gas at internal sites such as cracks or voids, form chemical compounds such as hydrides when combined with carbon or oxygen [6], or diffuse through the lattice as a screened proton.

Hydrogen may be present in all three forms at the same time in the same material, each one giving rise to a particular set of properties. Each of these forms may degrade the properties of the metal.

The location of hydrogen in a metal is varied and a distinction must be made between lattice diffusing hydrogen and trapped hydrogen. In general, hydrogen will be trapped by crystal defects where it is energetically favorable for the interaction to occur. Various traps such as cracks, voids, grain boundaries, dislocations, substitutional atoms, and second phase particles have been identified, and in some instances their interaction energy with hydrogen has been measured [6,12].

2.3 Theories of Hydrogen Embrittlement

The term, hydrogen embrittlement, is used to describe the damaging effects of hydrogen on a metal, both in the presence and absence of external stress. For a hydrogen charged metal sample which is subjected to an external tensile stress, the degradation of mechanical properties is generally expressed in terms of the loss of ductility. Hydrogen embrittlement manifests itself in unstressed metal by forming blisters and internal cracks.

Several of the theories which have been proposed to explain hydrogen embrittlement will be briefly described.

2.3.1. The Pressure Theory

In 1940 Zapffe and Sims [13] proposed that the formation of high hydrogen gas pressures in internal cavities is responsible for the embrittling effect of hydrogen. While this is the reason for a number of static failures [14], it is inconsistent with the observation that hydrogen embrittlement may exist when the internal hydrogen concentration is too low for the formation of high pressure gas [15]. Moreover, it does not explain the role of diffusing or trapped atomic hydrogen in the nucleation of cracks and internal cavities.

2.3.2. The Reduction of Cohesive Energy

In this theory, originally proposed by Troiano [10] and further developed by Oriani [16], hydrogen is believed to concentrate in the lattice at points of maximum triaxial stress, where it reduces the binding energy between the metal atoms. The fact that hydrogen may concentrate at the high stress region near a crack tip is well documented experimentally and theoretically [17,18]. The hypothesis that the cohesive energy will be decreased remains without strong theoretical basis since little is known about binding energies in crystals. However, there is experimental evidence to show that internal hydrogen reduces the elastic modulus of iron [19].

2.3.3. The Reduction of Surface Free Energy

This model developed by Petch [20] is a special case of the

cohesive energy model. The difference between the two models resides in the location of hydrogen at the crack tip. The surface energy model assumes that hydrogen atoms are absorbed on the internal surface of the crack rather than in the metal lattice, thus reducing the surface energy and the energy required for crack propagation.

2.3.4. The Trap Theory

Recently, Pressouyre [8] has developed this theory based on the results of hydrogen trapping experiments and hydrogen trapping models which have been developed since the existence of hydrogen traps was first proposed by Darken and Smith [11]. In this model, a critical concentration of hydrogen at a particular site is required in order for any damaging effects to occur. Moreover, the susceptibility of any material to hydrogen embrittlement is directly related to its trap populations. Reversible traps are thought to play a dual role, namely that of a hydrogen source or of a sink. The prevailing role will depend on the following:

1. Whether the hydrogen is in the metal prior to the test, or if it is introduced into the metal during the test.
2. The mode of hydrogen transport through the lattice (as dislocation atmospheres, by interstitial jumps in the lattice, or along short-circuit paths such as grain boundaries and dislocations which are oriented parallel to the hydrogen flux).

Experimental evidence has shown that each of the first three mentioned theories seems to explain the hydrogen embrittlement phenomenon for selected instances. However, the trap theory appears to be very promising since it has been used to explain much of the seemingly contradictory behavior of materials in the presence of internal hydrogen [8]. It also yields information which indicates when the other theories are applicable.

2.4 Diffusion Models

2.4.1. Simple Diffusion Theory

The concentration of hydrogen, $c(x,t)$, diffusing in a homogeneous metal lattice of thickness, a , is determined by the diffusion equation:

$$\frac{\partial C}{\partial t} = D_0 \frac{\partial^2 C}{\partial x^2}, \text{ for } 0 < x < a; \quad 2.1$$

where $C = C_0$ at $x = 0$, and $C = 0$ at $x = a$ for $t > 0$; $C = 0$ for all x at $t = 0$. Where $t =$ time, and D_0 is the lattice diffusion coefficient which is assumed not to be a function of the hydrogen concentration or the specimen thickness.

The quantity of hydrogen,

$$Q(t) = \int_0^t [D_0 \frac{\partial C}{\partial x}]_{x=a} dt \quad 2.2$$

which has permeated through the metal in time t approaches an asymptote of slope $C_0 D_0 / a$ as t tends to infinity. An extrapolation of the plot of quantity against time gives the time lag, t_{lag} ,

which is related to the diffusion constant, D_o , by

$$t_{lag} = a^2/6D_o. \quad 2.3$$

It has been shown [21] that the time lag may be obtained by locating the time at which the permeation flux is 0.6299 times the steady state value.

Another method of determining the diffusion coefficient is to use the breakthrough time, t_b . This is the fastest method since one does not need the whole permeation transient. Moreover, it should be independent of any concentration effect since the hydrogen atoms should initially cross a hydrogen-free matrix. However, it may be an underestimate if there is a slow surface reaction for hydrogen entry into the material. The expression for t_b is:

$$t_b = a^2/15.3D_o. \quad 2.4$$

The effect of a slow surface reaction can be accounted for by subtracting the time required for the permeation current to begin to decay once the cathodic current is shut off. This time, called the relaxation time, t_r , can be measured in the manner shown in Figure 1. The effect of a slow surface reaction is better understood when one considers that the diffusion equations refer to the hydrogen concentration within the membrane and not the surface concentration on the membrane. When the galvanostat current is switched off the surface coverage changes in a time interval in the order of microseconds [22], but the concentration of hydrogen within the membrane requires a much

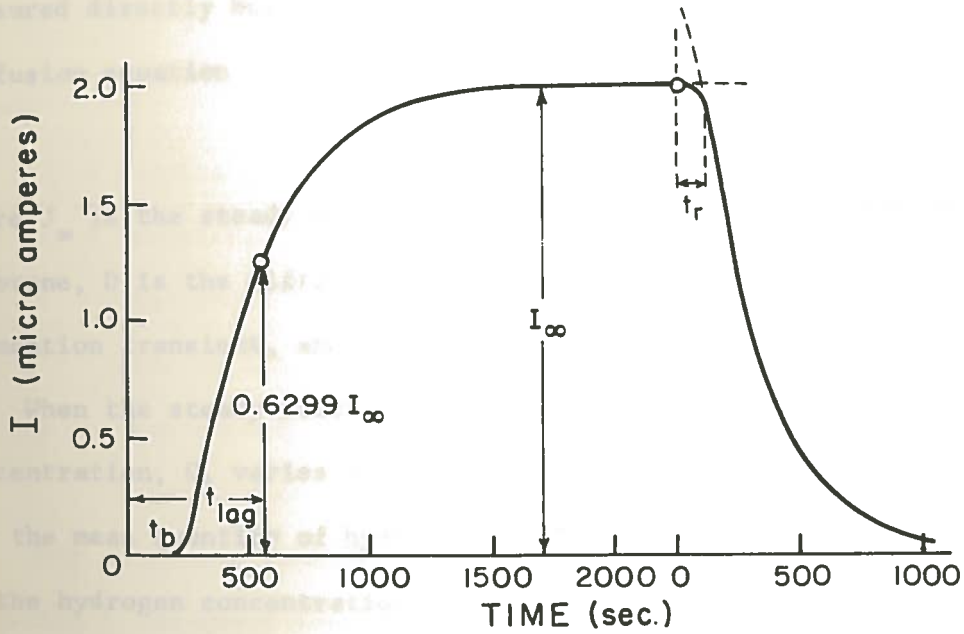


Figure 1: Typical Permeation Transient Showing Experimentally Measured Parameters.

longer time to adjust. The time of relaxation can thus be regarded as being due to a finite rate constant for the transfer of hydrogen atoms from the surface into the metal.

The input surface hydrogen concentration, C_0 , cannot be measured directly but it can be obtained from the steady state diffusion equation

$$J_{\infty} = DC_0/a, \quad 2.5$$

where J_{∞} is the steady state flux of hydrogen exiting from the membrane, D is the diffusion coefficient calculated from the permeation transient, and 'a' is the membrane thickness.

When the steady state flux of hydrogen is attained, the concentration, C , varies linearly throughout the specimen, and Q_0 , the mean quantity of hydrogen in the metal is $\frac{1}{2}C_0$, where C_0 is the hydrogen concentration at the input surface of the metal.

2.4.2. Diffusion Behavior with Trapping

In 1948 Darken and Smith [11] experimentally determined the quantity of hydrogen in steel to lie in the range of 0.8 to 0.85 times C_0 for certain values of C_0 . This was the first indication that a significant quantity of hydrogen can be trapped in a metal.

To account for the experimental observation of Darken and Smith, McNabb and Foster [23] modified the simple diffusion equations presented above. This was done to include the case of a uniformly distributed population of traps or potential wells

with varying capacities for capturing and delaying hydrogen atoms as they diffuse through the metal lattice. The rate equation for trapping is developed from straightforward probability considerations as

$$\frac{\partial n}{\partial t} = k C_L (1 - n) - pn, \quad 2.6$$

where

C_L = lattice hydrogen concentration;

n = fractional occupancy of traps ($0 \leq n \leq 1$);

k = mean probability for hydrogen transport from a lattice site to a trap;

p = mean probability of hydrogen escape from a trap to a lattice site.

For sheet membranes with the same boundary conditions as Equation 1, an exact solution for the time lag with trapping, t_t , was shown to be:

$$t_t = t_{lag} \left\{ 1 + \frac{3\alpha}{\beta} + \frac{6\alpha}{\beta^2} + \frac{6\alpha}{\beta^3} (1 + \beta) \ln(1 + \beta) \right\}, \quad 2.7$$

where t_{lag} is the time lag for purely lattice diffusion. The parameters α and β are specified by:

$$\alpha = N_T k/p, \text{ and} \quad 2.8$$

$$\beta = C_O k/p = n/(1 - n) \quad 2.9$$

where N_T is the trap density and C_O is the lattice hydrogen concentration at the input surface of the metal membrane.

In order to make this model applicable to experimental

data the limiting cases of Equation 7 should be examined. For mildly reversible hydrogen traps ($\beta, n \ll 1$) it has been shown that

$$\frac{t_t}{t_{lag}} = 1 + N_T k/p. \quad 2.10$$

For essentially irreversible traps ($n \cong 1, \beta \gg 1$)

$$\frac{t_t}{t_{lag}} = 1 + \frac{3\alpha}{\beta} = 1 + \frac{3N_T}{C_o}. \quad 2.11$$

Equations 10 and 11 can be rewritten in terms of the lattice diffusion coefficient, D_o , and the diffusion coefficient with trapping, D , as:

$$D_o/D = 1 + N_T k/p \quad \text{for } (\beta, n \ll 1) \quad 2.12$$

and

$$D_o/D = 1 + \frac{3N_T}{C_o} \quad \text{for } (n \cong 1, \beta \gg 1). \quad 2.13$$

Equations 12 and 13 are the solutions for the extremes of Equation 7 which range from mildly reversible to irreversible hydrogen traps. In both cases, and for all intermediate trapping situations, the diffusion coefficient with trapping is smaller than the lattice diffusion coefficient. For the case of mildly reversible hydrogen traps described in Equation 12 the diffusion coefficient with trapping decreases as the number of traps, N_T , increases and also as the capture to release ratio, k/p , increases. It has been shown by Caskey and Pillinger [24] that as the magnitude of these parameters increases the shape of the permeation transient departs from that of lattice diffusion, and the

transients require an increasing amount of time to reach steady-state.

The lattice diffusion coefficient, D_0 , where no trapping is present can be determined by using the equation which Gonzalez [25] obtained by compiling the available high temperature steady-state permeation data for high purity iron. At high temperatures the reversible and irreversible traps in iron become essentially inoperative because their trapping energy is insignificant compared to the energy possessed by the diffusing hydrogen atom. Thus, the hydrogen atom can jump from a trap as easily as it can jump from an interstitial lattice site. The Gonzalez equation states that:

$$D_0 = 0.78 \times 10^{-3} \exp(-1900/RT) \text{ cm}^2/\text{sec} \quad 2.14$$

where,

D_0 = lattice diffusion coefficient,

R = ideal gas constant (1.98 cal/mol^oK), and

T = temperature in degrees Kelvin.

The Gonzalez equation can be extrapolated to determine the room temperature diffusion coefficient for pure iron which contains neither trapping sites nor grain boundary short circuit paths for the rapid diffusion of hydrogen.

2.5 Characterization of Hydrogen Traps

When a hydrogen atom jumps from a normal lattice site into the neighborhood of a trap, the probability of an eventual return

to the former site is reduced. A force of attraction (usually characterized as a binding energy) between the hydrogen atom and the trap tends to retain the hydrogen in the vicinity of the trap. The four primary types of thermodynamic forces which can act on a diffusing hydrogen atom are due to electrical fields, stress fields, temperature gradients, or are chemical potential forces resulting from concentration gradients or the tendency to form chemical bonds. An example of an electrical force is the force exerted on hydrogen by any defect which introduces an electron vacancy into the lattice. The negatively charged electron vacancy will attract the screened hydrogen proton by electrostatic attraction. Forces exerted on the hydrogen proton by stress fields originate from defects in the lattice such as dislocations, coherent and semi-coherent grain boundaries, inclusions, and crack tips. Temperature gradients exert an attractive force on hydrogen since their presence biases the diffusional jump direction of hydrogen and provides a concentration gradient due to a solubility gradient. This increases the diffusion rate and solubility of hydrogen in steel. The chemical potential gradient is a function of the activity coefficient of hydrogen in iron. The chemical potential may then be expressed as a function of solute concentrations using interaction coefficients, where an attractive force exists between the trap and hydrogen when the interaction coefficient is negative. This means that the hydrogen proton will tend to form a compound with

the solute atom in iron, and that the solute atom is acting as a hydrogen trap.

The two distinct types of hydrogen traps which can exist in a crystal lattice are attractive and physical traps [26]. Attractive traps are thermodynamic in nature and have been described above. Physical traps are the result of modifications of the ideal crystal lattice, resulting in features where it is energetically more favorable for hydrogen to stay. A purely physical trap would trap hydrogen by its presence in the path of the diffusing hydrogen proton and not by a thermodynamic driving force directing the path of the diffusing proton to it. Nearly all traps are mixed in nature; for example, a void in the matrix is a physical trap, but its existence produces an electronic perturbation in the metal lattice.

In general, hydrogen traps which are mainly physical in nature act as irreversible traps and those which are mainly attractive in nature act as reversible traps. The reason for this is that only small, very probable, jump increments are needed to get out of an attractive trap, while a hydrogen atom has to leave a physical trap in one jump which is much less probable. Degassing experiments bear this out in that reversible traps release hydrogen continuously; whereas, irreversible traps release hydrogen only after a critical temperature is reached. The critical temperature is that at which the probability of a single jump out of an irreversible trap becomes non-negligible.

2.6 The Thermodynamic Force Between Sulfur and Hydrogen

The room temperature solubility of sulfur in iron is very small [27] but it is necessary to look at the interaction energy between sulfur in iron and lattice dissolved hydrogen. The simplest way of demonstrating the existence of a thermodynamic driving force is to look at the sign and amplitude of the first order interaction coefficient between sulfur and hydrogen.

The activity, a_i , of component i in solution in iron is given by:

$$a_i = f_i (\%i) \quad 2.15$$

where f_i = activity coefficient of i in iron and $\%i$ is its weight percent. The activity coefficient, f_i , is also related to the other elements dissolved in iron but the effect is generally quite small for small concentrations and to a good approximation:

$$\log f_i = \sum_j e_i^j (\%j). \quad 2.16$$

Here, j designates every element dissolved in iron (including i), e_i^j = first order interaction coefficient between j and i , and $(\%j)$ = weight percent of j in iron.

The important point is that e_i^j is related to the affinity that exists between elements i and j in iron. A negative e_i^j indicates a thermodynamic attraction between i and j , while a positive e_i^j is indicative of a thermodynamic repulsion between the two. The more negative e_i^j the stronger the attraction, and vice-versa. The first order interaction coefficient between

sulfur and hydrogen in iron has been measured [28,29,30] at 1600°C and it is a positive number which indicates repulsion between sulfur and hydrogen. As the temperature is decreased the interaction coefficient decreases. No room temperature data on the interaction coefficient between sulfur and hydrogen in iron is available in the literature.

2.7 Hydrogen Embrittlement in Steels Containing Sulfide Inclusions

Recently, Iino [9] has studied the effect of sulfur content in linepipe steel on the time to failure, the hydrogen induced fracture behavior, and the hydrogen evolution behavior of hydrogen charged tensile specimens. The alloy microstructure consisted of ferrite and pearlite with pearlite banding. Elongated manganese sulfide inclusions were found in the cross-section in quantities which corresponded to the sulfur content in the steel. Hydrogen induced fracture was observed to initiate at manganese sulfide inclusion-matrix interfaces.

All specimens were charged with hydrogen at 8mA/cm^2 in a 5 percent sulfuric acid solution containing a poison which delayed the rate at which atomic hydrogen formed molecular hydrogen.

At all stress levels it was observed that for hydrogen charged tensile specimens under static loading the time to failure was greatest for specimens containing 0.001 weight percent sulfur. Metallurgical examinations revealed that manganese sulfide inclusions were not yet formed at this low sulfur content. The

time to failure of hydrogen charged tensile specimens under static load decreased to a minimum value for sulfur contents slightly above the room temperature solubility of sulfur in steel. The time to failure then increased linearly with increasing sulfur content. A possible reason for this behavior is that a portion of the hydrogen entering the metal due to hydrogen charging diffuses toward the regions of maximum triaxial stress. In this case the sites of maximum triaxial stress are at the tips of the elongated manganese sulfide inclusions. Since the number of manganese sulfide inclusions increases with increasing sulfur content, the traps compete with one another for the available hydrogen in the metal. Therefore, at any one time the quantity of hydrogen trapped at manganese sulfide inclusions is smaller for alloys with higher sulfur content. It requires a longer period of time for a critical concentration of hydrogen to accumulate at the sulfides in alloys of higher sulfur content than in alloys with lower sulfur content. This is in accord with the Trap Theory of Hydrogen Embrittlement which hypothesizes that a critical concentration of hydrogen is required at a particular site before hydrogen damage can occur. In this case hydrogen damage manifests itself in the form of hydrogen induced fracture.

The fracture behavior in hydrogen charged steel under conditions free of external stress was found to be quite different from that observed under stress. Under these conditions fracture

extends faster with higher sulfur content.

Hydrogen evolution studies showed that with increasing sulfur content both unstressed and externally stressed tensile specimens contained increasing amounts of trapped hydrogen. In addition, for all except the alloys with the lowest sulfur content (0.001%S) externally stressed tensile specimens contained more trapped hydrogen than did unstressed samples.

The results of Iino's research indicate that manganese sulfide inclusions in linepipe steel act as irreversible hydrogen traps, and their presence in the metal may induce reversible trapping. Irreversible trapping is in the form of high pressure hydrogen gas located at the manganese sulfide-matrix interface. Hydrogen evolution studies indicate that reversible trapping is a function of both the quantity of manganese sulfide inclusions and the stress level. This, along with the Reduction in Cohesive Energy Theory of Hydrogen Embrittlement indicates that reversible hydrogen trapping sites are located in the iron matrix near the maximum triaxial stress region at the tip of the elongated manganese sulfide inclusions.

CHAPTER III

EXPERIMENTAL

3.1 Alloy Preparation

3.1.1. The Phase Diagram of the Fe-S System

For reasons developed in the Introduction, the base material of this study will consist of pure α -iron to which specific quantities of sulfur will be added. The relevant portion of the binary Fe-S phase diagram [31] in Figure 2 shows that sulfur exists in solid solution as a substitutional element in ferrite in quantities up to 0.02% at 914°C. However, the solid solubility decreases rapidly as the temperature decreases. During the freezing of iron, sulfur precipitates as a sulfide and since the Fe-S system freezes in a eutectic manner [32], the sulfur must concentrate in the liquid metal to the eutectic composition before the first sulfide is formed. It follows then that the sulfides will be located where the last metal solidified, namely at the primary grain boundaries or dendritic fillings.

3.1.2. Chemical Composition of the Alloys

Three Fe-S alloys containing low, medium and high sulfur contents were made with sulfur contents in the range found in

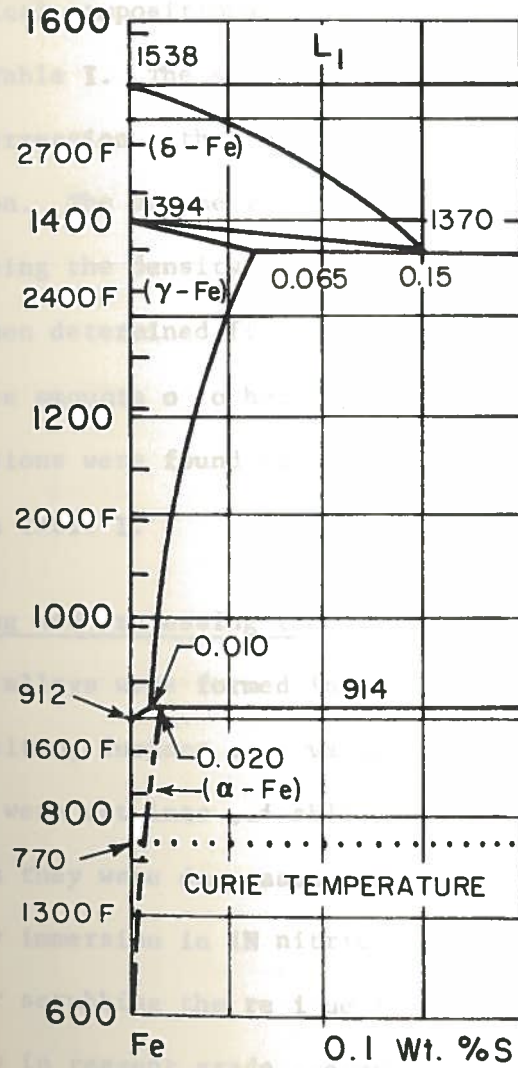


Figure 2. A Portion of the Iron-Sulfur Phase Diagram [31].

commercial steels. All alloys were made from high purity iron (99.999%Fe) rod and high purity sulfur (99.999%S) obtained from ESPI (Electronic Space Products Incorporated).

The chemical compositions of the alloys used in this study are given in Table I. The sulfur analysis was performed using the chord-intersection method of determining the iron-sulfide volume fraction. The volume fraction was converted to weight fraction by using the density of both iron and FeS. The sulfur content was then determined from the binary Iron-Sulfur phase diagram. Trace amounts of other impurity elements in the iron-sulfide inclusions were found by x-ray fluorescence and are also listed in Table I.

3.1.3. Melting and Processing the Alloys

The Fe-S alloys were formed into ingots using an NRC Model 2940 vacuum melting furnace at a vacuum of 3×10^{-5} torr. First, the iron rods were cut into suitable lengths for the melting crucible, then they were degreased and the surface oxide layer was removed by immersion in 1N nitric acid for approximately one minute. After scrubbing the residue from the iron it was cleaned ultrasonically in reagent grade acetone to remove any particles clinging to the metal. The iron was then rinsed in methyl alcohol and hot air dried. This rigorous cleaning procedure was used in order to ensure that an alloy with a minimum amount of contaminants was obtained. The iron rods were then weighed and an appropriate amount of sulfur was poured into a hole drilled

TABLE I

Chemical Composition of the Iron Alloys
Used in This Study.

| * Alloy | S (wt%) | Trace Elements (identified by x-ray fluorescence) |
|---------|------------|--|
| 3 | 0.003 | Cr, Al, Si, and Mn. |
| 9 | 0.009 | Cr, Al, Si, and Mn. |
| 13 | 0.013 | Cr, Al, Si, and Mn. |

* The alloy numbers correspond to the sulfur content ($\text{wt}\% \text{S} \times 10^{-3}$).

into the end of one of the iron rods. The hole was then pressed shut between the jaws of a vise. A piece of clean high purity iron protected each side of the iron rod from being contaminated by rust, grease, etc., from the vise jaws. Sealing the sulfur in the iron rod allowed the alloying element to react with or diffuse into the iron prior to melting. It also prevented the sulfur from vaporizing due to its low vapor pressure and the furnace being operated at a medium vacuum and high temperatures.

All alloys were melted in zirconia crucibles obtained from ESPI. These crucibles are non-reactive with and are not wetted by molten iron. A commercial purity graphite subseptor was used to buffer the crucible against thermal shock from the tungsten heating element.

After cooling to room temperature the ingots were compressed using a compression testing machine until they were thin enough to fit between the rolls of a hand rolling mill. The Fe-0.003%S and Fe-0.013%S alloys were then alternately cold-rolled and annealed at 800°C for one hour until a final thickness of approximately 1mm was obtained. The Fe-0.009%S alloy was annealed at approximately 700°C for thirty minutes between similar cold-rolling steps. After the final rolling operation the alloys were annealed at 800°C for one hour and allowed to cool to room temperature at a rate of less than 5°C/min. The mechanical processing history of each alloy is listed in Table II.

During cold-rolling all of the alloys developed processing

Table II: Mechanical Processing History of Fe-S Alloys

Fe-0.003 wt pct S Fe-0.009 wt pct S Fe-0.013 wt pct S

Alloy Composition

| Reduction No. | Percent Reduction in Area Between Annealing Operations | | |
|---------------|--|---------|------|
| 1 | 19% | No Data | 24% |
| 2 | 76% | No Data | 40% |
| 3 | *70% | 12% | *50% |
| 4 | --- | 9% | --- |
| 5 | --- | 23% | --- |
| 6 | --- | 30% | --- |
| 7 | --- | *33% | --- |

*No further processing beyond this point.

cracks which initiated at the edges of the metal and then extended into the alloy as it was cold-rolled. Permeation membranes were selected from uncracked portions of the alloy.

3.2 Microstructural Analysis Techniques

3.2.1. Preparation for Microstructural Examination

For each permeation specimen the grain size, number and shape of sulfide inclusions, the extent of internal cracking, and other metallurgical defects were determined by optical and scanning electron microscopy. Metallographic examinations were carried out using a Versamet Metallograph and an ISI-60A Scanning Electron Microscope. Each specimen was sectioned, mounted in Koldmount resin, then ground and polished. Grinding was done with silicon carbide papers through a grit size of 600 mesh. After being ground, the mounted specimens were polished using polishing wheels with diamond paste through $1.0\mu\text{m}$. Final polishing was done using a polishing wheel with $0.05\mu\text{m}$ aluminum oxide. Specimens were rinsed with methyl alcohol, hot air dried, cooled to room temperature and, if required, etched using either 2% Nital or Super picral etchant. All etching residue was removed by scrubbing the specimen with a cotton swab under running water. Etched specimens were then rinsed in methyl alcohol and hot air dried prior to microstructural examination.

3.2.2. Grain Size

The grain size of each Fe-S alloy sheet was measured normal to the biaxial rolling direction using the Lineal Intercept

Procedure described in ASTM E112 [33]. The grain size was measured normal to the biaxial rolling plane because the fully annealed metal had larger grains at the boundaries than in the mid-thickness region of the sheet. This is possibly a result of the greater driving force for grain growth at the boundaries of the metal. The larger driving force for grain growth is due to non-uniform deformation during cold-rolling resulting in the surfaces and edges being deformed to a greater extent than the mid-thickness of the metal.

3.2.3. Internal Cracking

Since internal cracking of all metal sheets occurred during cold-rolling, it was necessary to examine the microstructure of each membrane. Metallurgical examination revealed that nearly all cracks were oriented parallel to the biaxial rolling plane. In order to view the edges of the internal cracks it was necessary to section the membranes normal to the biaxial rolling plane.

3.2.4. Sulfide Inclusions

All of the alloys contained a relatively scant distribution of mainly spherical iron-sulfide inclusions which were located either at grain boundaries or within the grains.

The measurement of the volume of sulfide inclusions per unit volume of alloy was determined by quantitative microscopy as described by Hilliard [34]. The quantity of sulfide inclusions

was determined by the chord-intersection technique. This included examining the specimens at regular intervals and counting the number and length of sulfide inclusions which intersected a randomly oriented line of known length. A scribed eyepiece in the microscope was used as the chord. The lineal fraction was shown to be equivalent to the volume fraction of one phase in a mixture.

It has been shown by Underwood [35] that the surface area of the iron sulfide inclusions can also be determined by using the chord-intersection technique. The surface area is given by:

$$A_s = 2N_L \quad 3.1$$

where,

A_s = iron-sulfide surface area, and

N_L = the number of intersections of the chord by FeS inclusions per unit chord length.

3.3 Experimental Techniques

3.3.1. The Apparatus

Permeation measurements were carried out using a sensitive electrochemical cell originally developed by Devanathan and Stachurski [22]. This technique involves introducing hydrogen into one side of a metal membrane and measuring the flux of hydrogen which leaves the other side of the membrane. The sensitivity of this technique is very high, and boundary conditions on the input and output surfaces are well known and remain constant for the duration of the experiment. This technique is

capable of measuring hydrogen concentration on the order of 10^{-12} moles. Figure 3 shows a schematic diagram of the experimental set-up. The permeation cell was composed of two teflon compartments which were separated by a metal membrane. Each compartment was filled with 0.1N NaOH solution prepared from deionized distilled water. A thermometer was inserted into the solution in each chamber, and zero grade hydrogen gas was bubbled through the solution in each chamber in order to keep the solutions as free of oxygen as possible. This was done because it has been found that dissolved oxygen detrimentally affects the reproducibility of the measurements [36]. The side of the membrane which faced the cathodic compartment played the role of the cathode while the platinized platinum counter electrode inserted in this compartment was the anode. This side of the membrane was cathodically polarized at a sufficient potential to generate hydrogen atoms at the metal surface. The hydrogen generation rate was maintained steady by a galvanostat circuit. The entire cell was tilted to allow easy escape of any gas bubbles which may accumulate on the cathode or input side of the membrane. Such an accumulation could reduce the extent of the cathodic reaction and thus reduce the number of hydrogen atoms which enter and diffuse through the membrane. The anodic side of the membrane faced the anodic compartment and played the role of the anode while the platinized platinum counter electrode inserted in this compartment was the cathode. A saturated calomel

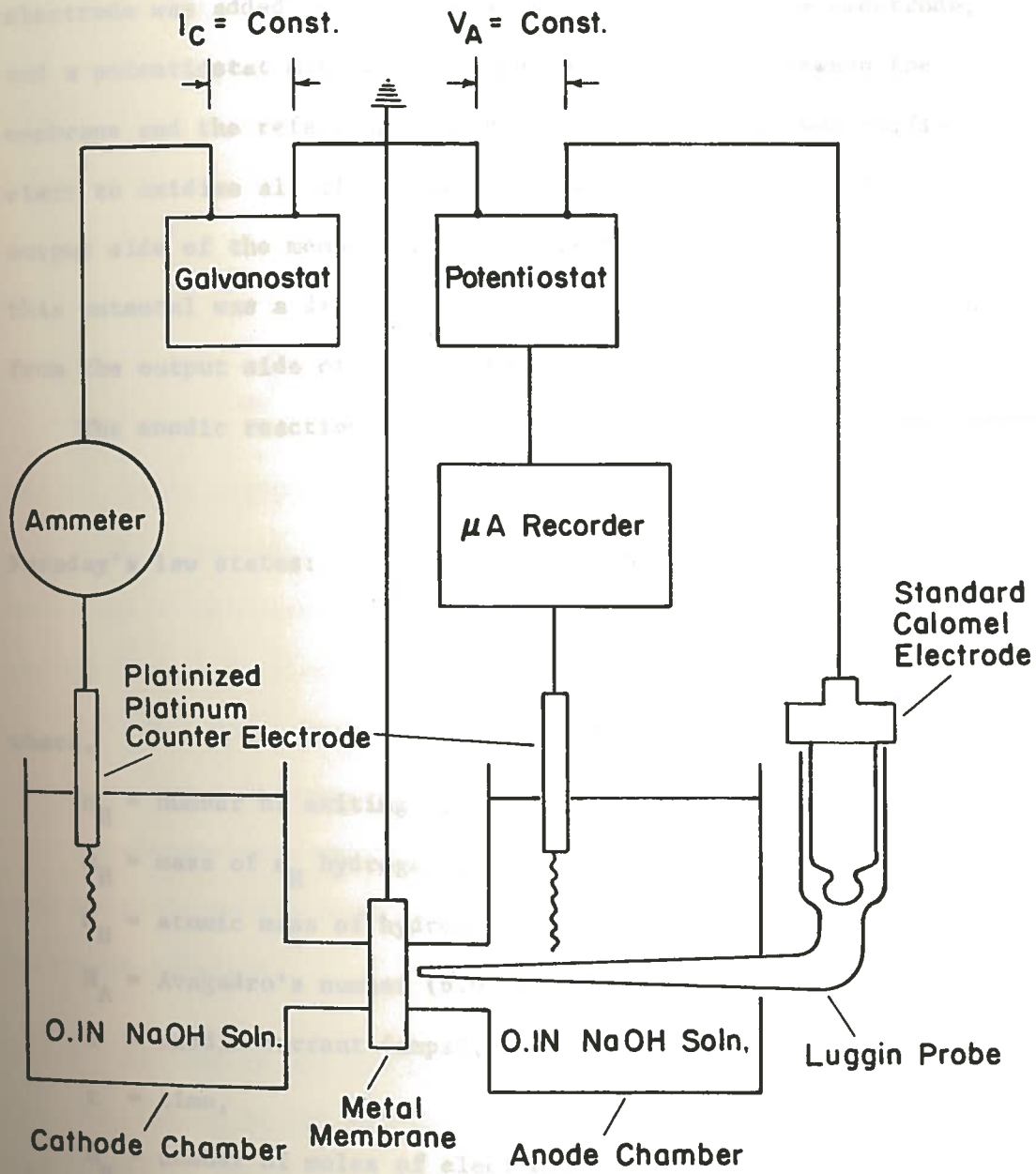
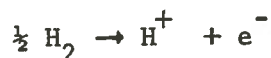


Figure 3: Schematic of Experimental Set-Up Used for all Permeations.

electrode was added to this compartment as a reference electrode, and a potentiostat maintained a constant potential between the membrane and the reference electrode. The potential was sufficient to oxidize all of the hydrogen exiting from the anode or output side of the membrane. The current necessary to maintain this potential was a direct measure of the flux of hydrogen exiting from the output side of the membrane.

The anodic reaction for the oxidation of hydrogen is:



Faraday's law states:

$$m_{\text{H}} = \frac{n_{\text{H}} M_{\text{H}}}{N_{\text{a}}} = \frac{M_{\text{H}} i t}{n_{\text{e}} F} \quad 3.2$$

where,

n_{H} = number of exiting hydrogen atoms,

m_{H} = mass of n_{H} hydrogen atoms,

M_{H} = atomic mass of hydrogen,

N_{A} = Avagadro's number (6.02×10^{23} atoms/mole of H),

i = anodic current (amps),

t = time,

n_{e} = number of moles of electrons required to oxidize a mole of hydrogen atoms,

F = Faraday's constant (96,500 amp x sec/mole of electrons).

The output flux of hydrogen, J_{H} , is given by:

$$J_{\text{H}} = \frac{n_{\text{H}}}{tA} = \frac{N_{\text{a}}}{n_{\text{e}} F} \cdot \frac{i}{A}, \quad 3.3$$

where A is the working area on the anode side of the membrane and the other terms are the same as above. Thus the output flux of hydrogen is proportional to the anodic current as:

$$J_H = \frac{N_a}{n_e F} \cdot \frac{i}{A} \quad 3.4$$

or

$$J_H \frac{\text{atoms}}{\text{cm}^2 \times \text{sec}} = 6.24 \times 10^{18} \times i(\text{amp})/A(\text{cm}^2). \quad 3.5$$

3.3.2. Other Accessories

A chart recorder was used to record the anodic current necessary to maintain a constant potential between the membrane and the standard calomel reference electrode.

A Fisher Model 620 electronic pH-meter was used for measuring the pH of the sodium-hydroxide solution.

An electrolytic cell consisting of a 4000 ml Pyrex beaker and two platinum electrodes was used for deionizing the sodium-hydroxide solution.

3.3.3. Setting Up the Experiment

a) Choice of the anodic potential. The anodic potential was chosen to ensure oxidation of all of the hydrogen exiting from the anodic side of the specimen. Table III shows that any potential more positive than the oxidation potential of hydrogen can do this. However, this positive potential will also oxidize iron, and the resulting current will not be a direct measure of

Table III: Oxidation Potentials from Handbook of Chemistry and Physics,
61st Edition, CRC Press.

| Reaction | E_{ox} (volts) |
|---|-------------------------|
| $2\text{H}_2\text{O} \rightleftharpoons \text{O}_2 + 4\text{H}^+ + 4\text{e}^-$ | 1.229 V |
| $\text{Pt} \rightleftharpoons \text{Pt}^{+2} + 2\text{e}^-$ | 1.2 V |
| $\text{Pd} \rightleftharpoons \text{Pd}^{+2} + 2\text{e}^-$ | 0.83 V |
| Saturated calomel electrode | 0.2415 V |
| $\text{H}_2 \rightleftharpoons 2\text{H}^+ + 2\text{e}^-$ | 0.000V |
| $\text{Fe} \rightleftharpoons \text{Fe}^{+3} + 3\text{e}^-$ | -0.036 V |
| $\text{Fe} \rightleftharpoons \text{Fe}^{+2} + 2\text{e}^-$ | -0.409 V |
| $\text{Fe}(\text{OH})_2 + \text{OH}^- \rightleftharpoons \text{Fe}(\text{OH})_3 + \text{e}^-$ | -0.56 V |
| $\text{H}_2 + 2\text{OH}^- \rightleftharpoons 2\text{H}_2\text{O} + 2\text{e}^-$ | -0.8277 V |

the amount of hydrogen leaving the membrane. In order to prevent this from happening, the output side of the membrane can be coated with a metal that is noble enough to withstand oxidation at the imposed anodic potential. The metal must also be quite permeable to hydrogen. Palladium was used to protect the membrane from anodic dissolution since its oxidation potential is much higher than that of iron ($E_{\text{ox}}^{\text{Pd}} = +0.83\text{V}$); the diffusivity of hydrogen in it is approximately $3.2 \times 10^{-7} \text{ cm}^2/\text{sec}$, and the solubility of hydrogen in palladium is much higher than in iron. In accordance with the above explanation the following limits have been put on the anodic potential:

$$+0.83\text{V} > E_{\text{anodic}} \text{ (ref.: H}_2 \text{ electrode)} > 0.0\text{V}$$

or

$$+0.5885\text{V} > E_{\text{anodic}} \text{ (ref.: Standard Calomel Electrode)} > -0.2415\text{V}$$

The sodium hydroxide solution was deionized, prior to being poured into the permeation cell for 24 hours at a potential of 6V, drawing a current of approximately 300mA. This was done in order to oxidize any impurity ions resulting from impurities in the sodium hydroxide pellets used to make the solution. If this were not done, reactions in the permeation cell would cause fluctuating currents which may be interpreted as oxidizing hydrogen. In addition, it would take longer for the residual current

to reach steady state.

b) Choice of cathodic current. The cathodic reaction $2\text{H}_2\text{O} + 2\text{e}^- \rightarrow \text{H}_2 + 2\text{OH}^-$ requires a cathodic potential greater than 0.8277 volts, with respect to the hydrogen electrode. When this potential is exceeded a wide range of current densities can be generated at the cathodic side of the membrane. As the cathodic current density is increased the quantity of hydrogen entering the membrane increases. If this quantity exceeds some critical concentration, irreversible cracking of the membrane occurs and permeation transients are not reproducible.

This side of the membrane was also palladium plated in order to prevent corrosion of the membrane which would cause a non-uniform distribution of hydrogen on the cathodic surface.

The cathodic current density was maintained at 0.8mA/cm^2 because this current density has been used with success by previous investigators [6,22]. Also, Pressouyre [6] has found that for experiments of long duration, contamination of the input surface was less at low current densities than at high current densities. Surface contamination can alter the shape of the permeation transients. Also, at high current densities, cracking can occur in the metal lattice or along grain boundaries. This has been found to profoundly affect the diffusion of hydrogen through the membrane since internal surfaces are known to trap hydrogen. In addition, cathodically protected steel structures are often protected using a cathodic current density of approximately

0.8 mA/cm².

c) Preparation of the specimen. One inch square permeation specimens were cut from the cold-rolled alloys which were approximately 1 mm thick. The membranes were then mechanically polished to a mirror-like finish. When the desired surface quality was obtained, wire leads were spot-welded to tabs extending from the membranes. The membranes were then prepared for palladium plating according to the following procedure which has been described previously [36]:

1. Specimens were degreased in benzene and wiped dry with cotton;
2. immersed and swabbed with cotton for one minute in a solution of 2% by volume of concentrated hydrochloric acid in reagent grade methyl alcohol; rinsed in methyl alcohol; hot air dried; cooled to room temperature;
3. immersed and swabbed with cotton for 3 minutes in a solution of 2% by volume of concentrated sulfuric acid in reagent grade methyl alcohol; rinsed in methyl alcohol; hot air dried; cooled to room temperature.

An electroless palladium coating was then applied immediately after this pre-treatment of the iron membranes. The specimen was dipped into the electroless palladium bath, described by Rhoda [37] as a bulk electroless plating bath, and left there for approximately 2 hours. The resulting layer of palladium was

smooth, crack free, and approximately 6×10^{-4} cm in thickness.

Using the diffusion rate of hydrogen through palladium as $D_{\text{Pd}}^{\text{H}} = 3.2 \times 10^{-7}$ cm²/sec, the time for a hydrogen atom to cross the palladium layer is approximately:

$$t = a^2/D_{\text{Pd}}^{\text{H}} = \frac{(0.006 \text{ cm})^2}{3.2 \times 10^{-7} \text{ cm}^2/\text{sec}} = 1.1 \text{ sec.} \quad 3.6$$

Thus, the protective layer is not considered a diffusion barrier.

After plating, each specimen was scrubbed with a stiff brush using soap and water, rinsed in methyl alcohol, hot air dried, and then clamped to the permeation cell between the teflon flanges which separate the two compartments.

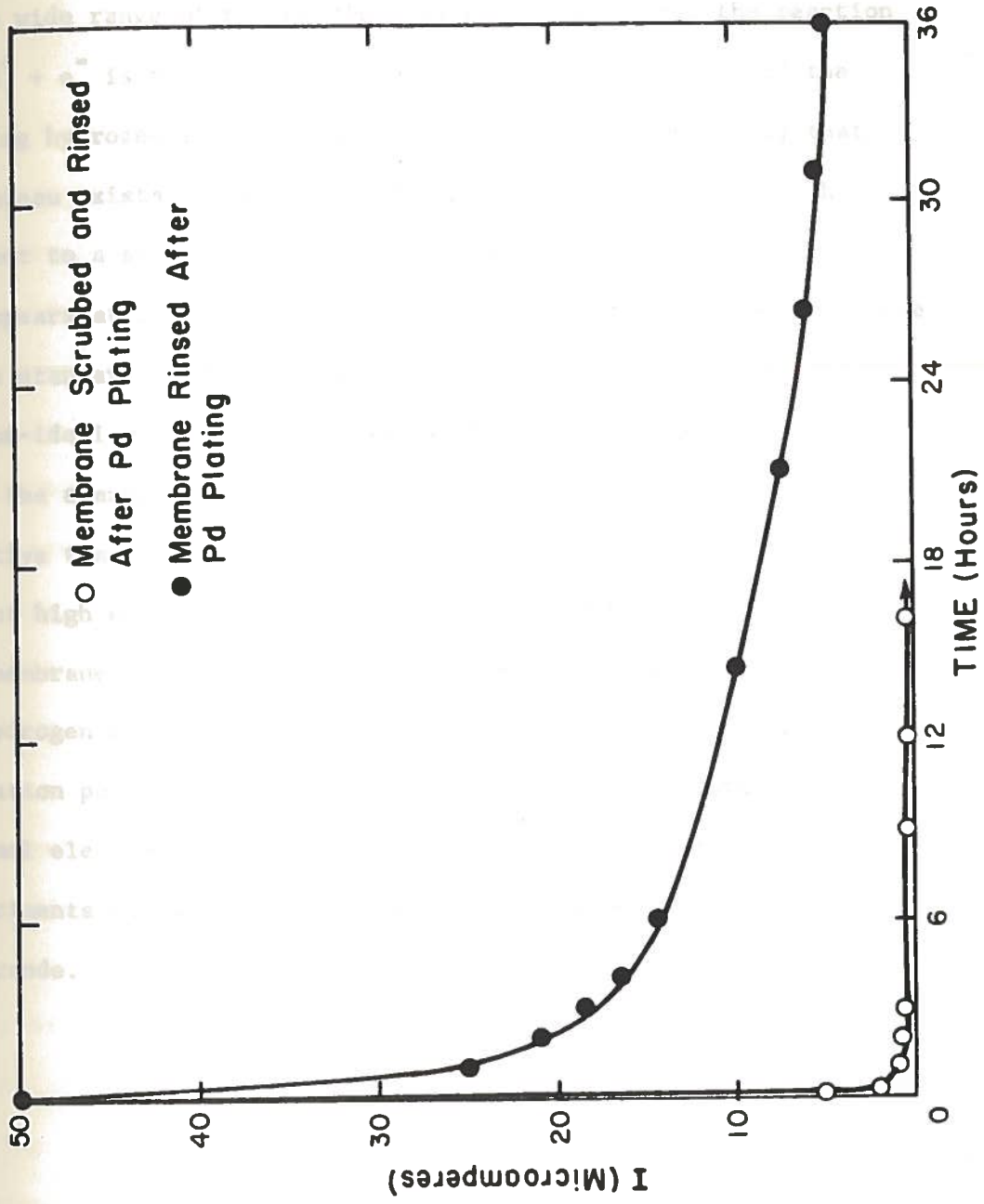
d) Preparation of the Solution. Conductivity grade water was made by filtering tap water using a Corning Water Purifier (model LD-5) with two inorganic impurity filters (#3508-B) in series. The water resistance was set at 500Ω . The filtered and deionized water was then distilled using a Corning Mega-Pure still. The 0.1N NaOH solution was prepared by dissolving 12.2 grams of Baker reagent grade sodium hydroxide (98.1% NaOH) in three liters of the conductivity water. The pH of the hydrogenated solution was 12.51.

e) First Trial. The permeation cell was set-up as described previously with the chart recorder in operation. All permeation experiments were carried out at room temperature, $25 \pm 2^\circ\text{C}$. The sodium hydroxide solution was poured into the anodic compartment and the anodic potential established. Permeation measurements were not started immediately because there existed a residual

current which stabilized to a steady state value of approximately $1\mu\text{A}/\text{cm}^2$ after about 24 hours. This residual current may have been due to conditioning of the palladium surface, desorption of hydrogen that may have been absorbed in the palladium layer during the plating operation, or due to the oxidation of various impurities dissolved in the solution. It is likely that a large portion of the residual current was due to conditioning of the palladium coating because both the time for residual current to decay and the steady state residual current was reduced by scrubbing the specimen with soap and water immediately after plating. The decay of the residual current is shown in Figure 4 for both scrubbed and unscrubbed specimens. After doing this the specimen was rinsed in methyl alcohol and hot air dried before being installed in the permeation cell. When the residual current reached equilibrium, sodium hydroxide was poured into the cathode chamber and several minutes were allowed to pass before starting permeation by turning on the cathode current. This was necessary since pouring the solution into the cell caused a small amount of movement of the cell which temporarily disturbed the electrical interface between the solution and metal surface on the anodic side of the membrane.

The effectiveness of the protective palladium layer was verified by varying the applied anodic potential and measuring the steady state flux of hydrogen. If the palladium is protecting the iron membrane from dissolution, one should see a constant

Figure 4. Decay of the Residual Current in the Anode Chamber.



value for the steady state flux of hydrogen through the membrane for a wide range of potentials. This indicates that the reaction $H \rightarrow H^+ + e^-$ is the only reaction occurring and that all of the exiting hydrogen is being oxidized. It has been shown [6] that a plateau exists between approximately -100mV and +500mV with respect to a saturated calomel electrode. The plateau disappears at $E_{\text{anodic}} > 500\text{mV}$ versus the standard calomel electrode for a standard oxidation reaction. However, since the solution is non-ideal with respect to pH and ion species, some deviation from the standard potential is expected. At potentials more negative than -100mV the plateau disappears because the potential is not high enough to oxidize the hydrogen which is exiting from the membrane. Once again, the cell potential where the oxidation of hydrogen no longer occurs will deviate from the standard oxidation potential of -241.5mV with respect to the standard calomel electrode. The anodic potential used for all permeation experiments was 400mV, with respect to the standard calomel electrode.

16
RAT.
00-
A. T.
FS=
10
BY
403LSEC
OFF
12
10

CHAPTER IV

RESULTS AND DISCUSSION

4.1 Microstructural Characterization

For all membranes the alloy microstructure consisted of iron-sulfide inclusions in an α -iron matrix. Inclusions and second phase particles other than FeS inclusions were not found. The iron-sulfide inclusions were identified using x-ray fluorescence, and the volume fraction of FeS in the iron was determined by the chord-intersection technique. The average sulfur content of each alloy was calculated and has been listed previously in Table I along with trace elements detected by x-ray fluorescence.

An x-ray fluorescence analysis of the metal matrix and sulfide inclusions found that iron was the only element detected in the matrix, while all impurity elements were located in the iron-sulfide inclusions. The FeS inclusions appeared to contain trace amounts of chromium, aluminum, silicon, and possibly manganese. Typical x-ray fluorescence spectra of iron grains and FeS inclusions are shown in Figures 5 and 6 respectively.

The only other defects found in the metal which was permeated by hydrogen were processing cracks and small numbers of pinholes which were a result of the melting and processing history.

16-NOV-81 00:05:10 STANDBY 43
RATE: CPS TIME 403LSEC
00-20KEV: 10EV/CH PRST: OFF
A: TEST6G B:
FS= 2500 MEM: A FS= 12

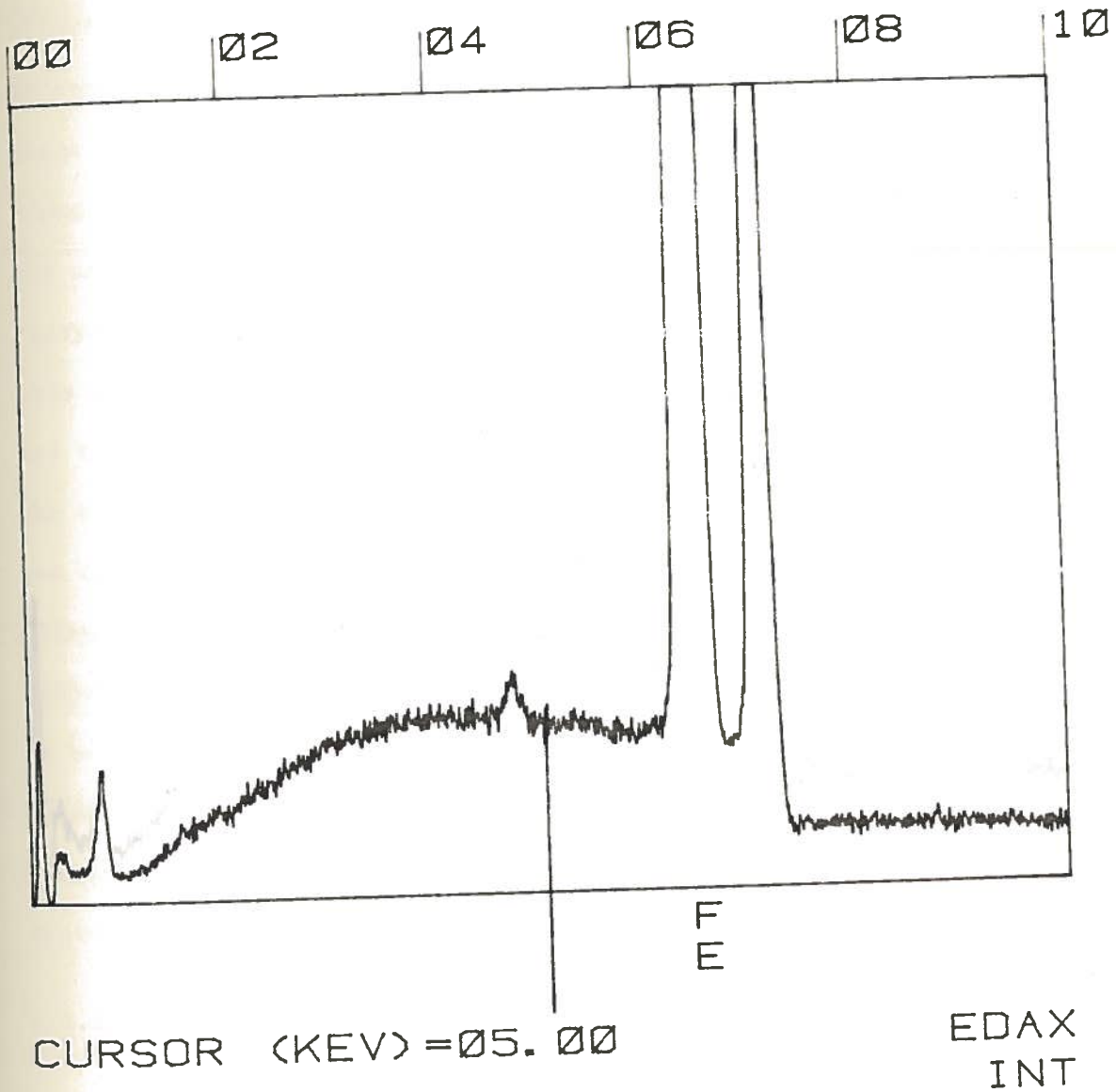


Figure 5. X-Ray Fluorescence Spectrum
of a Ferrite Grain.

16-NOV-81 00:20:34 STANDBY 44
 RATE: CPS TIME 288LSEC
 00-40KEV: 20EV/CH PRST: OFF
 A: TEST6S B:
 FS= 1614 MEM: A FS= 6

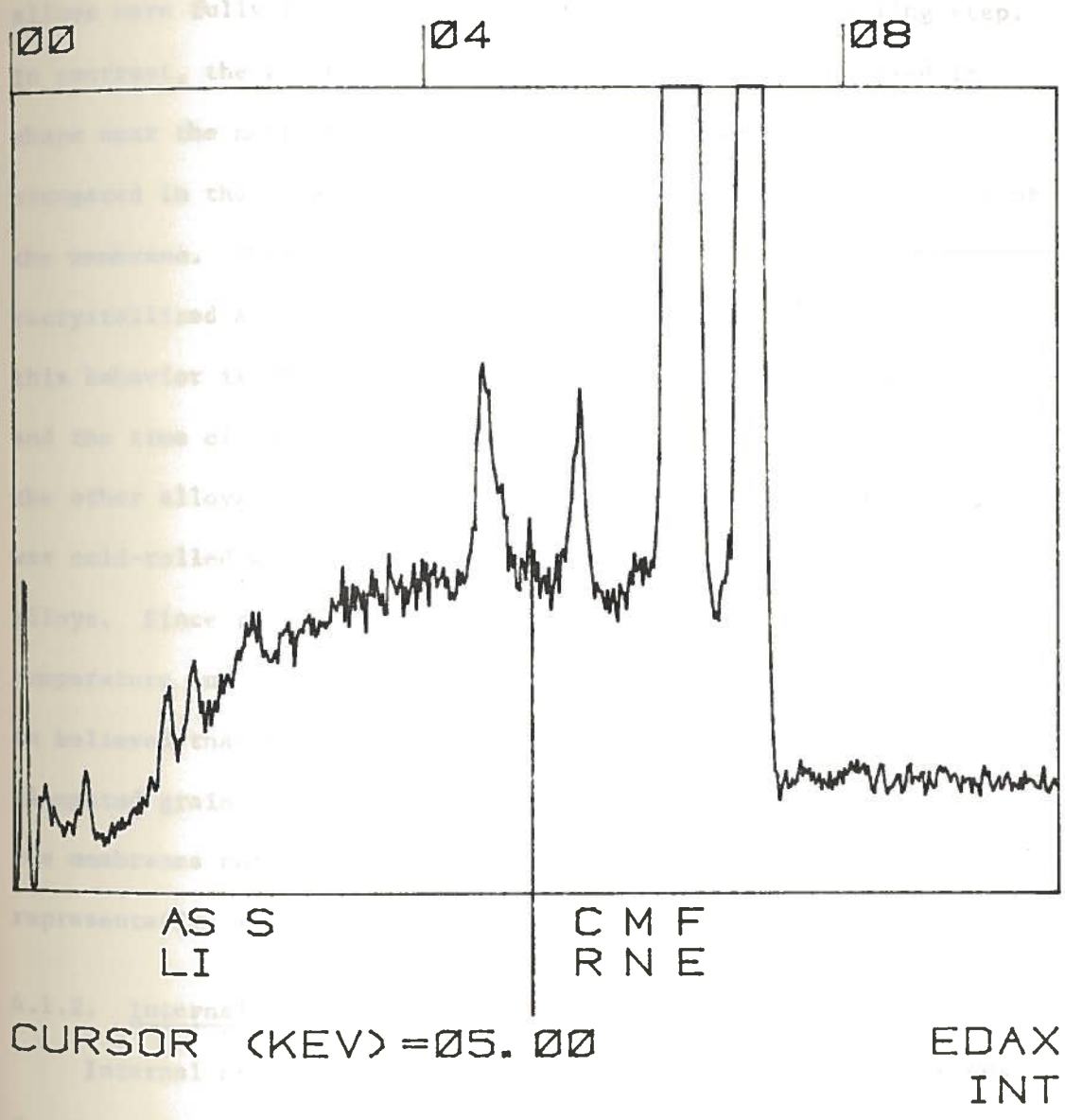


Figure 6. X-Ray Fluorescence Spectrum of an Iron-Sulfide Inclusion.

4.1.1. Grain Size and Shape

The grains of the Fe-0.003%S and Fe-0.013%S alloys were mainly equiaxed in shape and exhibited a slight decrease in size toward the mid-thickness region of all membranes. This indicates that the alloys were fully recrystallized after the final cold-rolling step. In contrast, the grains of the Fe-0.009%S alloy were equiaxed in shape near the metal surface but were much larger and highly elongated in the direction of cold-rolling near the mid-thickness of the membrane. This indicates that the alloy was not completely recrystallized after the final cold-rolling step. The reason for this behavior is probably twofold. First, the annealing temperature and the time of annealing was less for the Fe-0.009%S alloy than for the other alloys; and second, Table II shows that the Fe-0.009%S alloy was cold-rolled with smaller reductions in area than the other two alloys. Since recrystallization is highly dependent on the annealing temperature and the internal strain energy stored in the metal, it is believed that these two factors are responsible for the large elongated grains in the alloy. The average ferrite grain size for the membranes cut from each alloy is listed in Table IV and representative microstructures are shown in Figure 7.

4.1.2. Internal Cracking

Internal cracking occurred in some of the permeation membranes due to cold-rolling the alloy. This was verified by metallographic inspection of alloy samples which were not exposed to internal hydrogen. Internal cracks were found to be both intergranular

TABLE IV

Grain Size of Each Alloy Calculated
by the Lineal Intercept Procedure.

| Alloy Composition (wt%S) | Average Grain Size (microns) |
|-----------------------------|---------------------------------|
| Fe-0.003%S | 29 |
| Fe-0.009%S | 58 |
| Fe-0.013%S | 42 |

Figure 2. Repres-
Grain
Fe-0.013%
were at



(a)



(b)



(c)

Figure 7. Representative Micrographs of Fe-S Alloys Showing Grain Structures of (a) Fe-0.003%S Alloy, (b) Fe-0.009%S Alloy, (c) Fe-0.013%S Alloy. All specimens were etched with Super picral etchant, 100X.

and transgranular in nature, and the plane of cracking was generally parallel to the rolling plane of the alloy.

The Fe-0.003%S and Fe-0.013%S alloys contained very few processing cracks (only one internal crack was found in six permeation membranes), while the Fe-0.009%S alloy contained large amounts of intergranular and transgranular cracking. Several of the internal cracks found in the alloys are shown in Figure 8.

4.1.3. Sulfide Inclusions

All permeation membranes contained a relatively small number of homogeneously distributed iron-sulfide inclusions which were located either at grain boundaries or within ferrite grains. The Fe-0.003%S and Fe-0.009%S alloys contained mainly spherical inclusions; whereas, the Fe-0.013%S alloy contained approximately equal quantities of both spherical and oblong FeS inclusions. In all alloys the inclusions varied from approximately 1.25 μ m to 5.0 μ m in diameter. Representative micrographs of sulfide inclusions are shown in Figure 9 for all alloys.

The volume fraction and surface area of the iron-sulfide inclusions were determined as was described previously. The volume fraction of FeS in iron is related to the weight fraction as:

$$V_v = \frac{w_{\text{FeS}} / \rho_{\text{FeS}}}{w_{\text{FeS}} / \rho_{\text{FeS}} + (1 - w_{\text{FeS}}) / \rho_{\text{Fe}}} \quad 4.1$$

where,

V_v = volume fraction of FeS in iron,

w_{FeS} = weight fraction of FeS in iron,



(a)



(b)



(c)

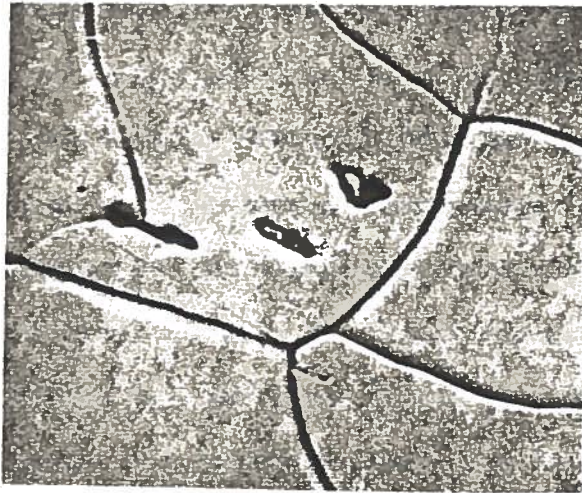
Figure 8. Representative Micrographs of Internal Cracking in Fe-S Alloys Showing (a) Transgranular Cracking in Fe-0.009%S Alloy, Super picral etchant, 1150X, (b) Intergranular Cracking in Fe-0.009%S Alloy, Unetched, 1000X, (c) Internal Crack in Fe-0.013%S Alloy, Unetched, 200X.



(a)



(b)



(c)

Figure 9. Representative Micrographs of FeS Inclusions in
(a) Fe-0.003%S alloy, Super picral etchant, 1500 X,
(b) Fe-0.009%S alloy, Super picral etchant, 800 X,
(c) Fe-0.013%S alloy, Super picral etchant, 1600 X.

ρ_{FeS} = density or specific weight of FeS, and

ρ_{Fe} = density or specific weight of iron.

The weight fraction of FeS was calculated from Equation 1 and used to determine the weight percent of sulfur in each iron alloy by employing the inverse lever rule and using the two-phase region of the iron-sulfur phase diagram. The average sulfur content of each alloy is shown in Table V along with the measured volume fraction and calculated surface area of FeS inclusions in each membrane.

4.2 Permeation Results

All experimental variables such as charging solution, cathodic current density, and anodic potential were kept essentially constant so variations in the observed diffusion behavior can be attributed to differences in the permeation membranes. A list of the experimental variables and the membrane thickness for each permeation test is given in Table VI. Also, the entry and exit sides of all membranes were palladium plated in order to ensure similar hydrogen entry and discharge conditions for all alloys.

In order to aid the analysis of the data and to make it easier to compare the shape of the transients, all permeation transients have been non-dimensionalized with respect to hydrogen flux. The normalized flux is shown in all figures as J/J_{∞} , where J is the instantaneous hydrogen flux and J_{∞} is the steady-state flux of hydrogen exiting from the permeation membrane.

The normalized flux is used for comparing successive permeation

Table V: Volume Fraction and Surface Area of Iron-Sulfide Inclusions Found in Each Permeation Membrane.

| Average Alloy Composition (wt %S) | Permeation Test No. | Volume Fraction of FeS Inclusions | Surface Area of FeS Inclusions (cm ² /cm ³) |
|-----------------------------------|---------------------|-----------------------------------|--|
| 0.003 | 3-1 | 1.5×10^{-4} | 2.4 |
| 0.003 | 3-2 | 4.3×10^{-5} | 0.7 |
| 0.009 | 9-1 | 3.8×10^{-4} | 3.0 |
| 0.013 | 13-1 | 6.0×10^{-4} | 10.0 |
| 0.013 | 13-2 | 5.9×10^{-4} | 8.8 |

Table VI. Experimental Conditions and Membrane Thickness for Each Permeation Experiment.

| Alloy Composition (wt %S) | Test No. | Membrane Thickness (cm) | Charging Solution | Anodic Potential (mV SCE) | Cathodic Current Density (mA/cm ²) |
|------------------------------|----------|-------------------------------|----------------------|------------------------------|--|
| Fe-0.003%S | 3-1 | 0.081 | 0.1N NaOH | 400 | 0.8 |
| Fe-0.003%S | 3-2 | 0.094 | 0.1N NaOH | 400 | 0.8 |
| Fe-0.009%S | 9-1 | 0.092 | 0.1N NaOH | 400 | 0.8 |
| Fe-0.013%S | 13-1 | 0.101 | 0.1N NaOH | 400 | 0.8 |
| Fe-0.013%S | 13-2 | 0.104 | 0.1N NaOH | 400 | 0.8 |

transients for a membrane because slight variations in the steady-state flux are commonly observed.

4.2.1. Irreversible Trapping

The rise transients for the first and second polarization are shown in Figures 10 through 14 for the three Fe-S alloys studied. The permeation results indicate that both the breakthrough time and the time-lag are greater for the first transient than for the second. Successive polarizations produced transients which were very similar to the second polarization transient in all cases except when surface contamination was found on the cathodic side of the membrane after the permeation tests were completed. Surface contamination greatly affects the shape of the permeation transients and will be discussed.

The total quantity of hydrogen which has diffused out of the exit side of the membrane in time 't' is equal to the area under the flux-time curve. If the hydrogen entry conditions are the same for the first and second transient, the total quantity of irreversibly trapped hydrogen in the metal is simply the difference in the area beneath the first and second polarization transients. In this case, the time span is from the start of polarization to the time required for the first polarization permeation transient to attain a steady-state hydrogen flux from the output surface of the membrane.

The first polarization rise transients shown in Figures 10 through 14 are shifted to the right of the second transients.

Figure 10. Flux Normalized First and Second Polarization Permeation Transients for Fe-0.003%S Alloy (Test No. 3-1).

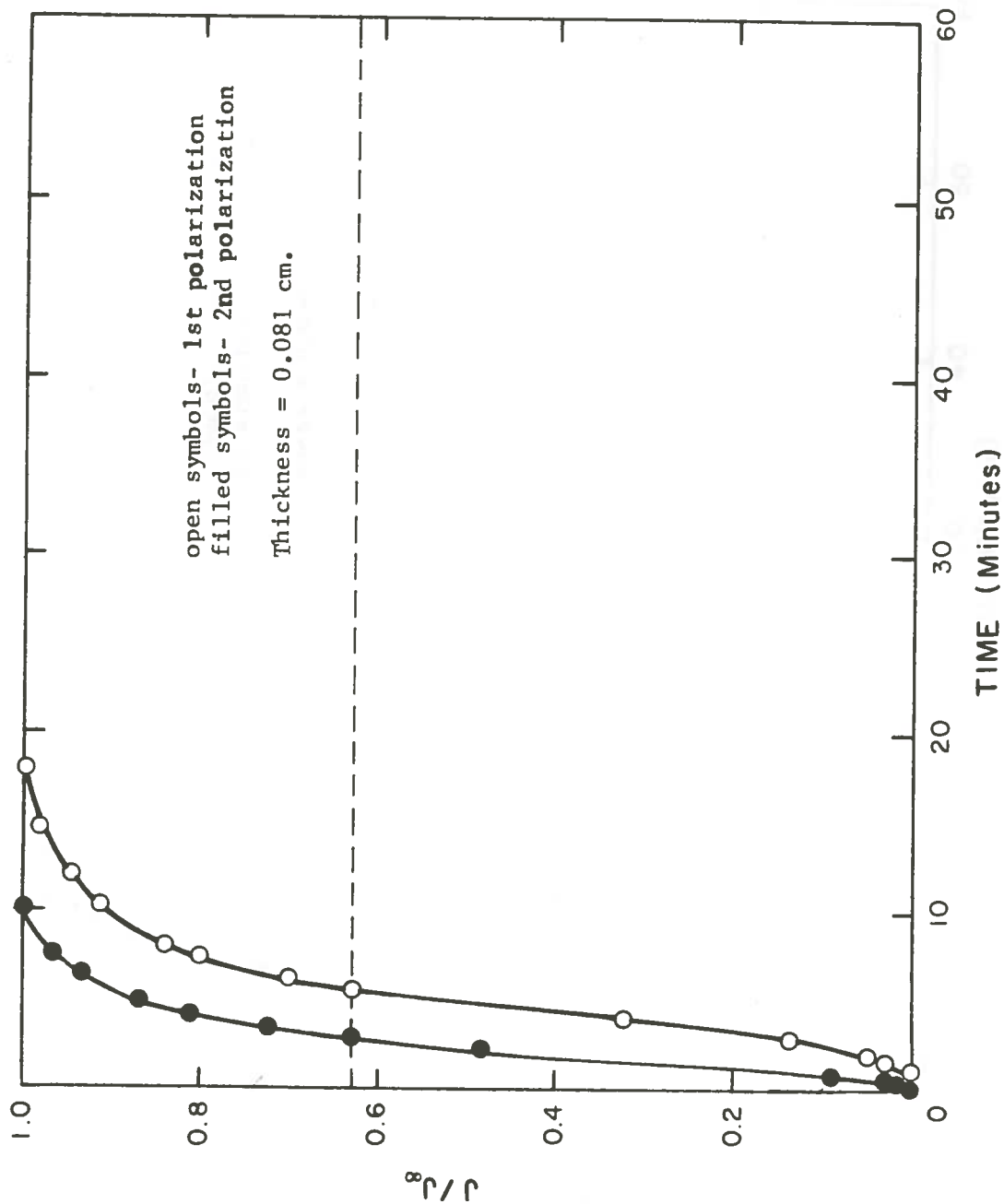


Figure 11. Flux Normalized First and Second Polarization Permeation Transients for Fe-0.003%S Alloy (Test No. 3-2).

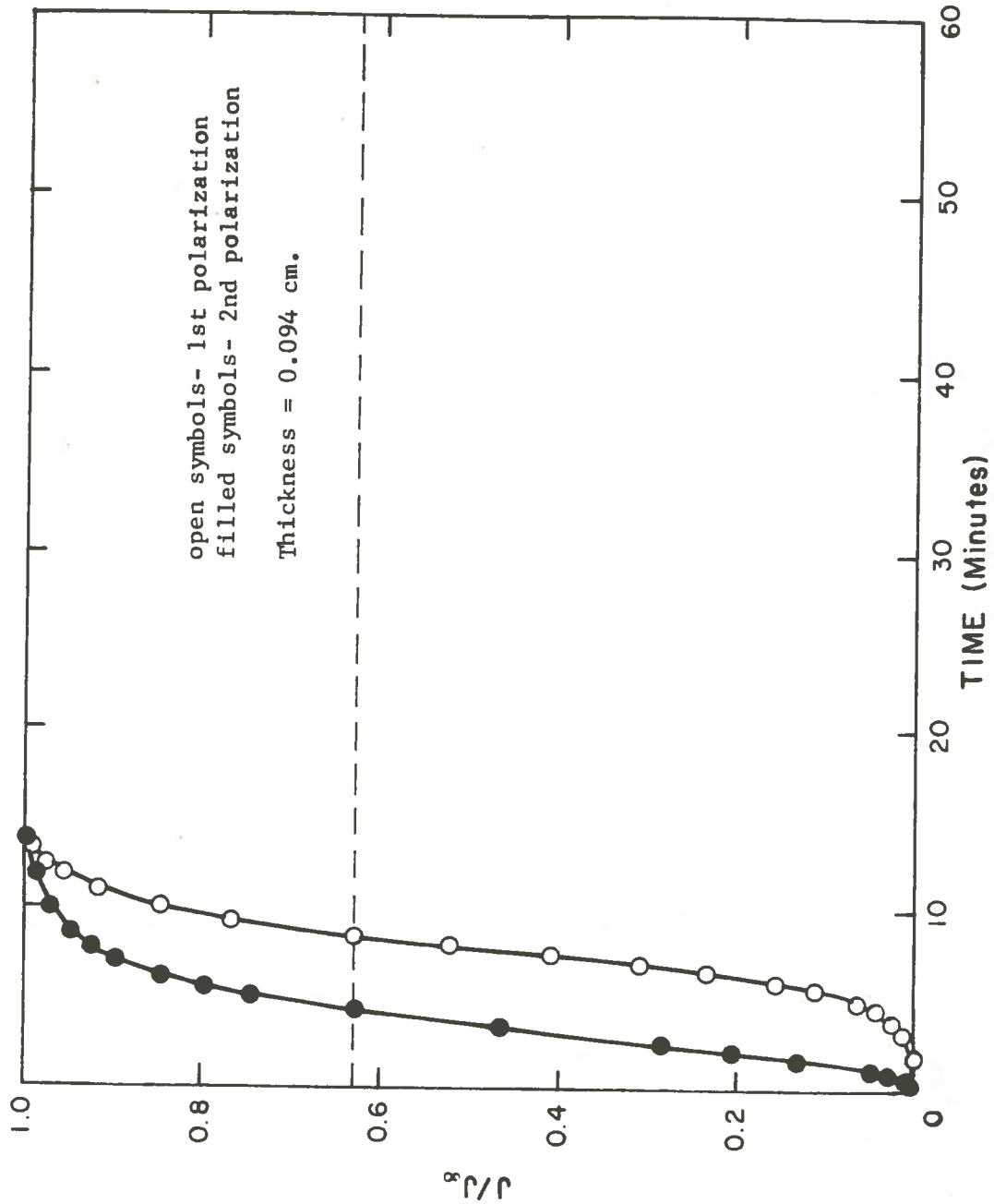


Figure 12. Flux Normalized First and Second Polarization Permeation Transients for Fe-0.009%S Alloy (Test No. 9-1).

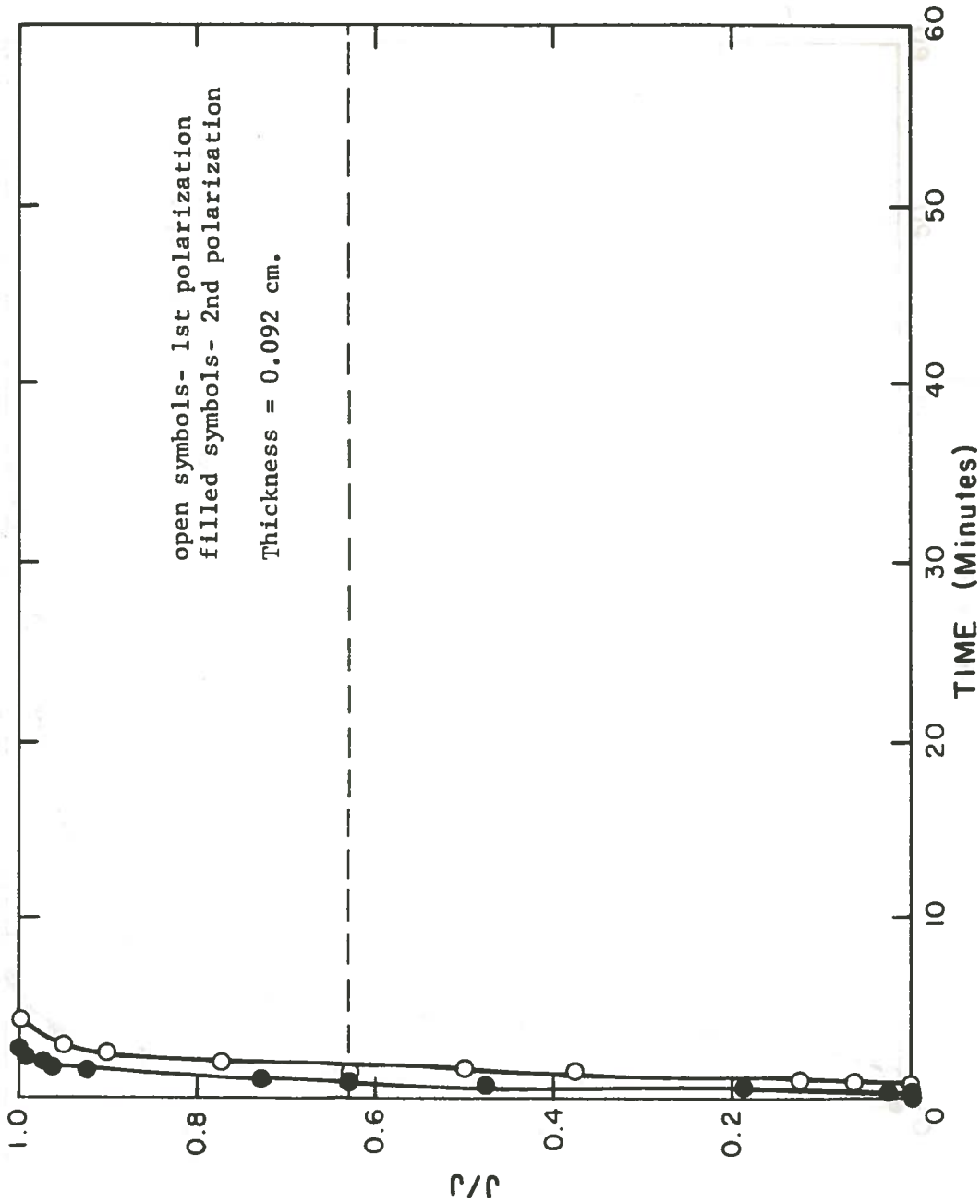


Figure 13. Flux Normalized First and Second Polarization Permeation Transients for Fe-0.013%S Alloy (Test No. 13-1).

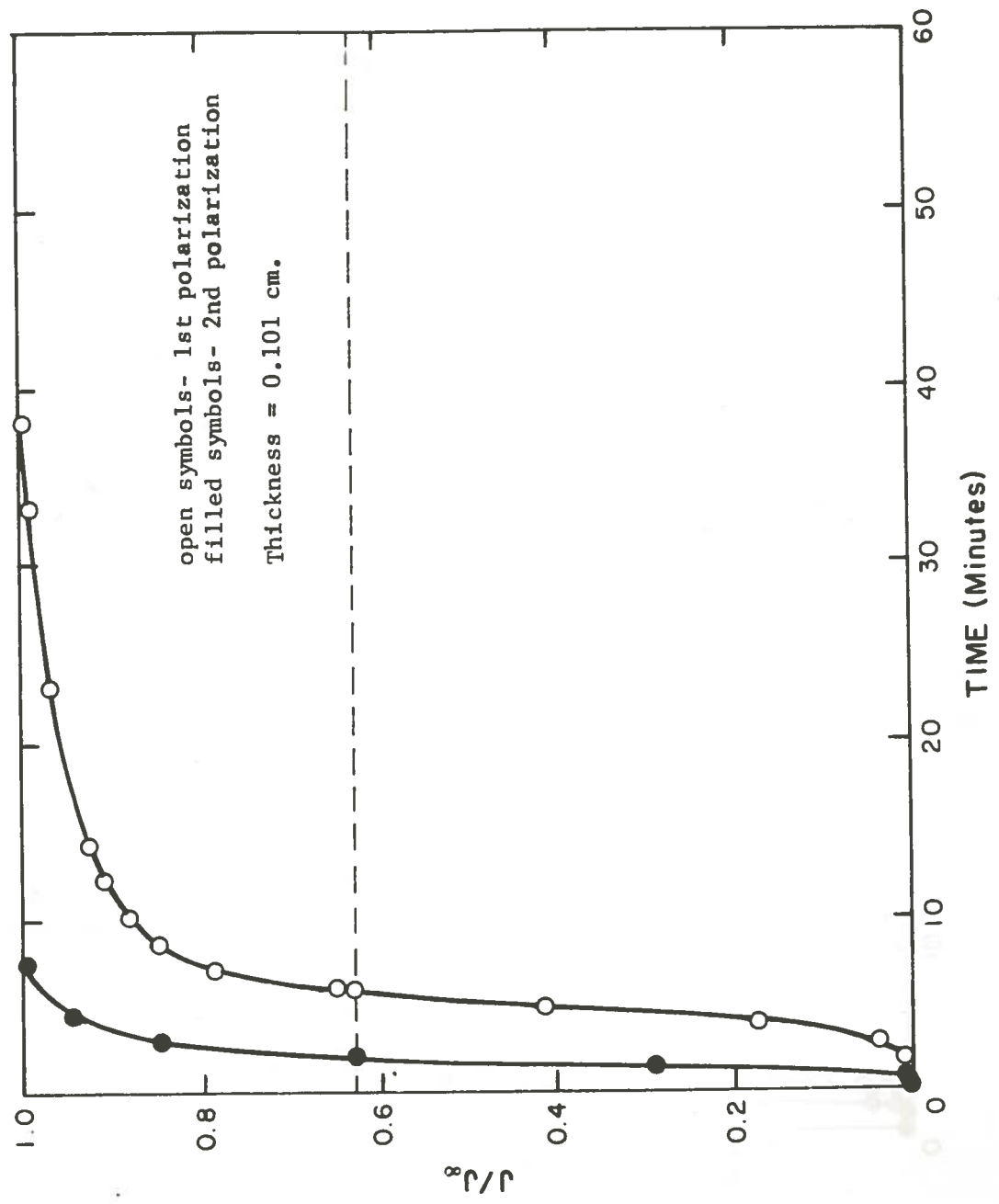
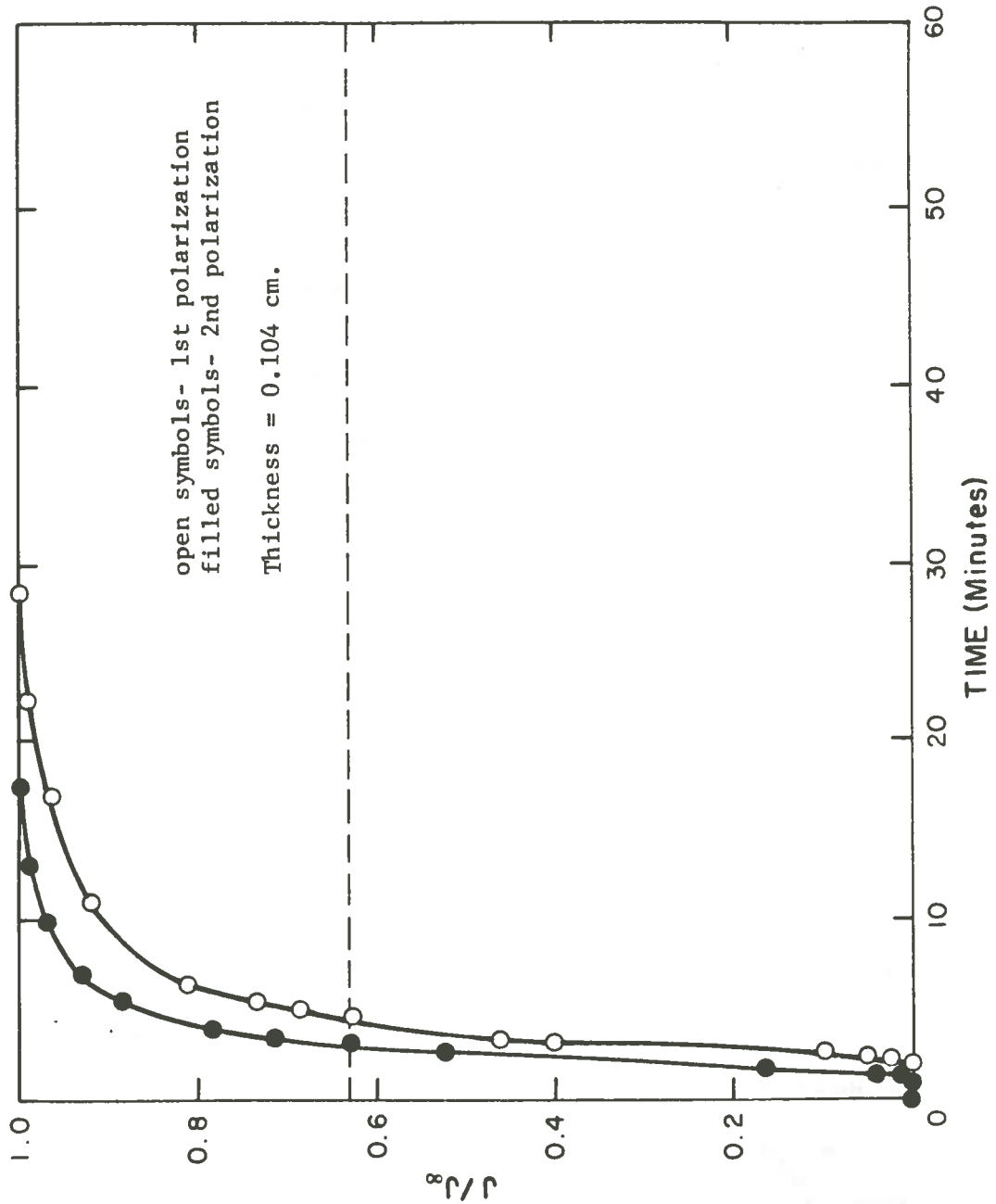


Figure 14. Flux Normalized First and Second Polarization Permeation Transients for Fe-0.013%S Alloy (Test No. 13-2).



This indicates that all membranes contained irreversible hydrogen traps which were initially free of internal hydrogen. These irreversible traps were filled during the first polarization and had no further interaction with diffusing hydrogen during successive polarizations. The similarity between the second and successive permeation rise transients indicated that all irreversible hydrogen traps were filled during the first polarization.

4.2.2. The Possibility of Short-Circuit Diffusion Paths

Figure 12 shows the first and second transient for the Fe-0.009%S alloy membrane. The first and second transients are very similar to each other. However, the first transient is shifted a small amount to the right of the second transient and this indicates that only a small amount of irreversible trapping occurred in this membrane. This does not seem plausible when one notes that both the lower and higher sulfur content alloys exhibited a greater amount of irreversible trapping than this intermediate sulfur content alloy.

Another unusual characteristic of this membrane is its high apparent diffusion coefficient. The apparent diffusivity of hydrogen was calculated from the time-lag and the breakthrough time equations using the permeation data and values of $D_{t_b} = 2.53 \times 10^{-5} \text{ cm}^2/\text{sec}$ and $D_{t_{lag}} = 2.65 \times 10^{-5} \text{ cm}^2/\text{sec}$ were obtained for the second polarization. These values are very similar to the lattice diffusivity of hydrogen in pure iron at room temperature

(25°C = 298°K) which can be calculated by extrapolating the Gonzalez equation (Eqn. 2.14) to yield

$$D_o = 3.12 \times 10^{-5} \text{ cm}^2/\text{sec.}$$

Such large values of the apparent diffusivity of hydrogen in fully annealed iron are not generally found at room temperature.

The absence of significant irreversible trapping and the high diffusion coefficient indicate that significant quantities of hydrogen may be passing through the metal membrane along short-circuit paths. Indeed, Figure 8 shows that such paths may exist in the Fe-0.009%S alloy membrane in the form of grain boundary cracks in the metal. Further analysis of the permeation of hydrogen through the Fe-0.009%S alloy membrane will not be attempted.

4.2.3. Surface Effects

Surface contamination in the form of deposited corrosion products on the cathodic surface of the membrane was never present at the start of the first polarization. This was determined by visually inspecting the surface of the membrane immediately prior to pouring the sodium hydroxide solution into the cathodic chamber of the permeation cell. In all cases the surface was uncontaminated. After the permeation tests were run it was noted, in a number of cases, that a medium to heavy gold colored deposit was found on the cathode surface of the membrane.

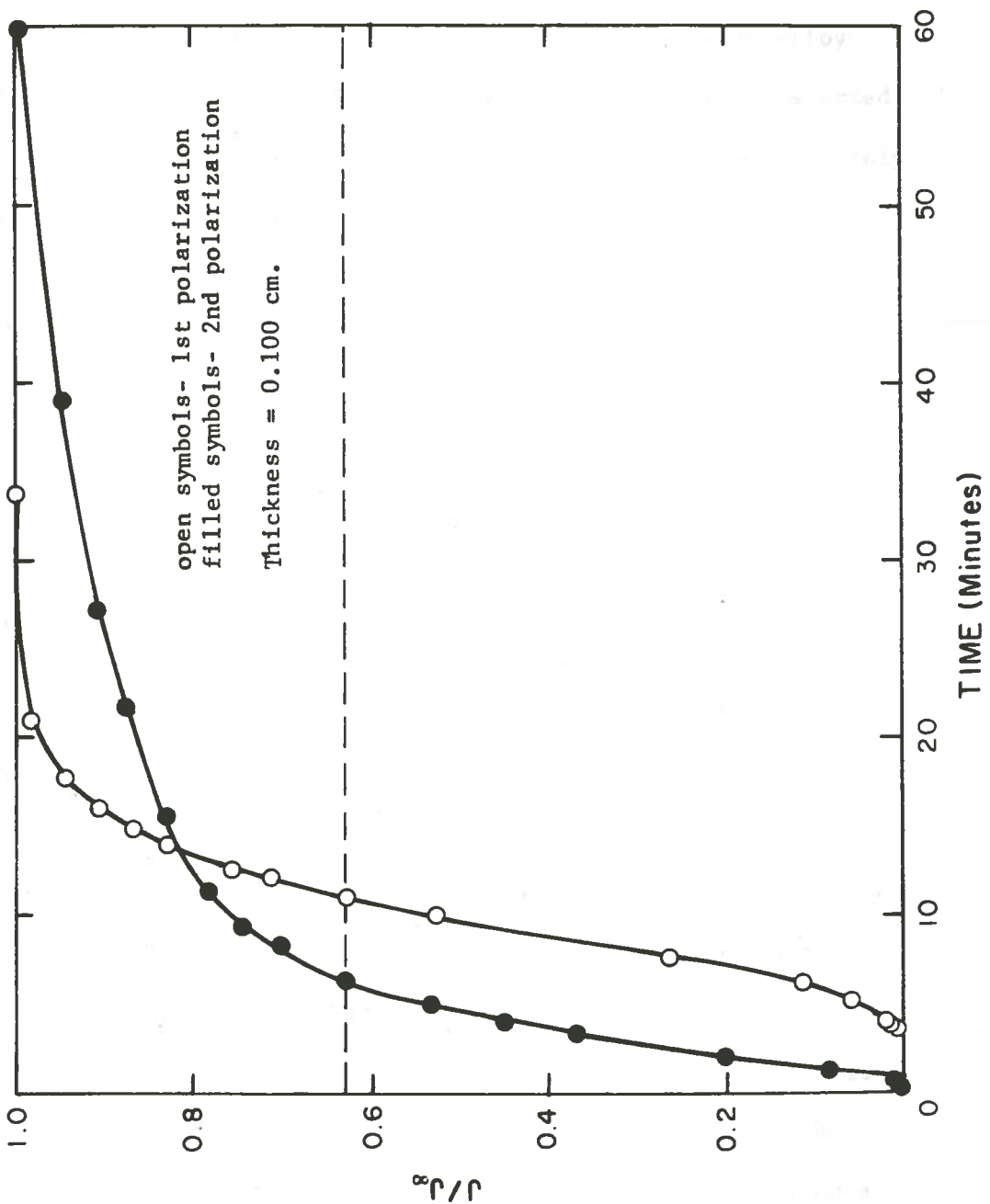
Surface contamination has been found to affect the shape of permeation rise transients in the following ways:

- 1) A large decrease in the steady state flux of hydrogen exiting from the membrane between successive permeation transients indicates that surface effects may be altering the entry of hydrogen into the metal;
- 2) a gradual decrease in the steady state flux during a polarization could indicate that surface contaminants are building up at the metal surface;
- 3) if the second permeation transient has a smaller positive slope than the first transient in the intermediate region of the curve it indicates that surface contaminants may be depositing on the metal surface;
- 4) an increase in the breakthrough time and time-lag between the second and successive transients could indicate that surface effects are reducing the quantity of hydrogen entering the metal;
- 5) a gentle upward sloping curve near the upper end of the second permeation transient resulting in it taking a longer time to reach steady-state than the first transient may indicate that the input surface is being contaminated and that hydrogen entry is being reduced.

During the permeation experiments all of the situations described above were encountered, and if visual examination of the membrane surface revealed surface contamination the results were discarded.

Figure 15 shows the effects which are likely to be observed

Figure 15. Effects of Input Surface Contamination on the First and Second Polarization Permeation Transients of an Fe-0.013%S Alloy.



when contaminants build up on the metal surface. The results show a first polarization permeation transient which is quite similar to the results obtained for other membranes of the same alloy type. The second polarization permeation rise transient started out looking quite normal; however, after it reached approximately half of its steady state flux the slope of the curve decreased rapidly and slowly approached steady state. Visual examination of the hydrogen input surface after the test revealed that a gold colored deposit was present on the metal surface.

4.2.4. Permeation Decay Transients

The permeation decay transients for the Fe-0.003%S and Fe-0.013%S alloy membranes are shown in Figures 16 through 19. The relaxation time was measured from the decay transients for each membrane and is listed in Tables VII and VIII along with the corrected and uncorrected apparent diffusion coefficients for the first and second transients respectively. As was mentioned previously, the relaxation time can be subtracted from the time-lag and breakthrough time to correct for slow surface reactions at the membrane surface. The results show that the diffusion coefficients are slightly increased when the relaxation time is subtracted from the time-lag and the breakthrough time. The results also show that the apparent diffusion coefficients have somewhat different values when calculated by the breakthrough time and time-lag methods. This is in line with the concept

Figure 16. Normalized Output Flux of Hydrogen versus Time for the Permeation Decay Transient of an Fe-0.003%S Alloy (Test No. 3-1).

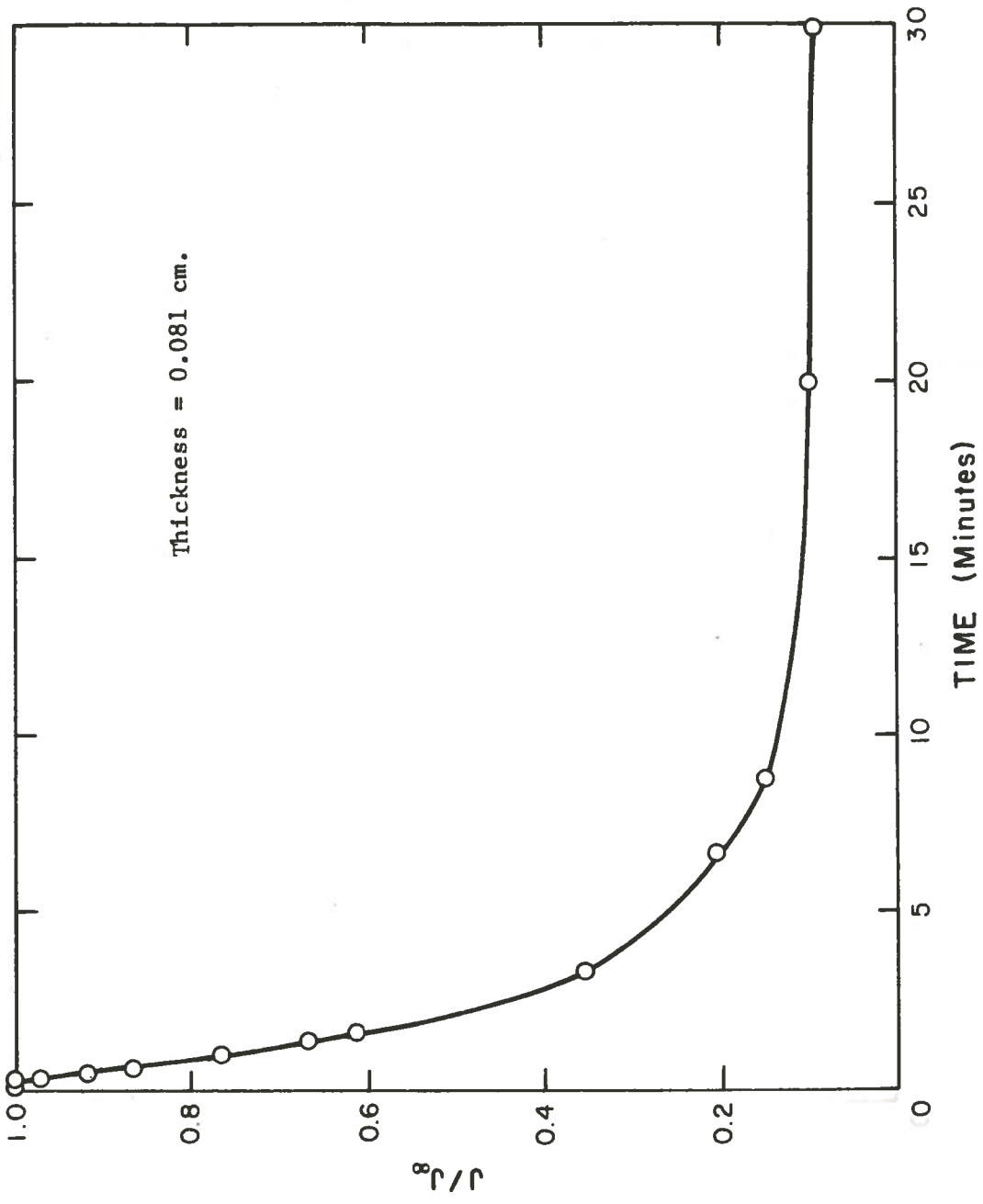


Figure 17. Normalized Output Flux of Hydrogen Versus Time for the Permeation Decay Transient of an Fe-0.003%S Alloy (Test No. 3-2).

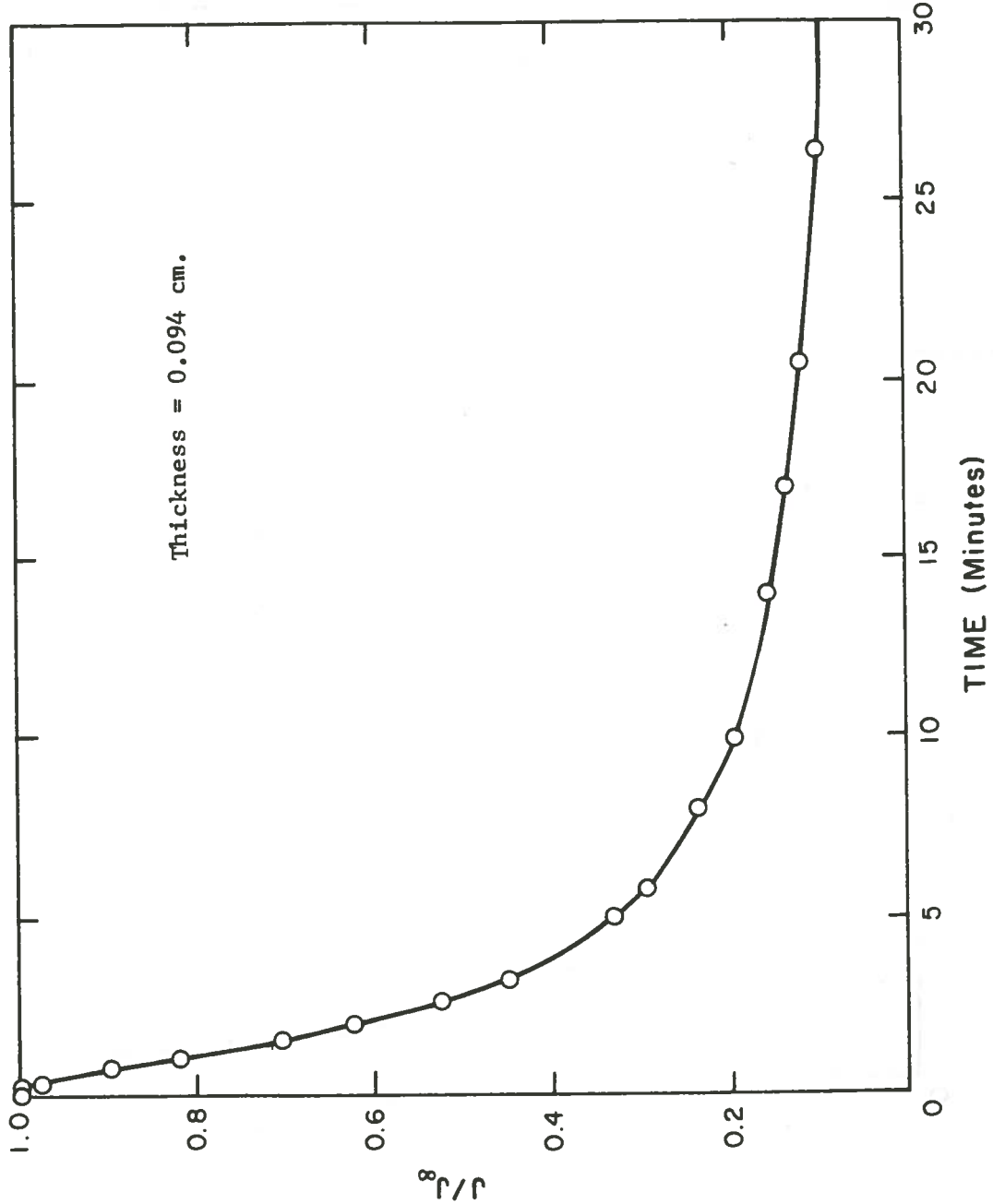


Figure 18. Normalized Output Flux of Hydrogen Versus Time for the Permeation Decay Transient of an Fe-0.013%S Alloy (Test No. 13-1).

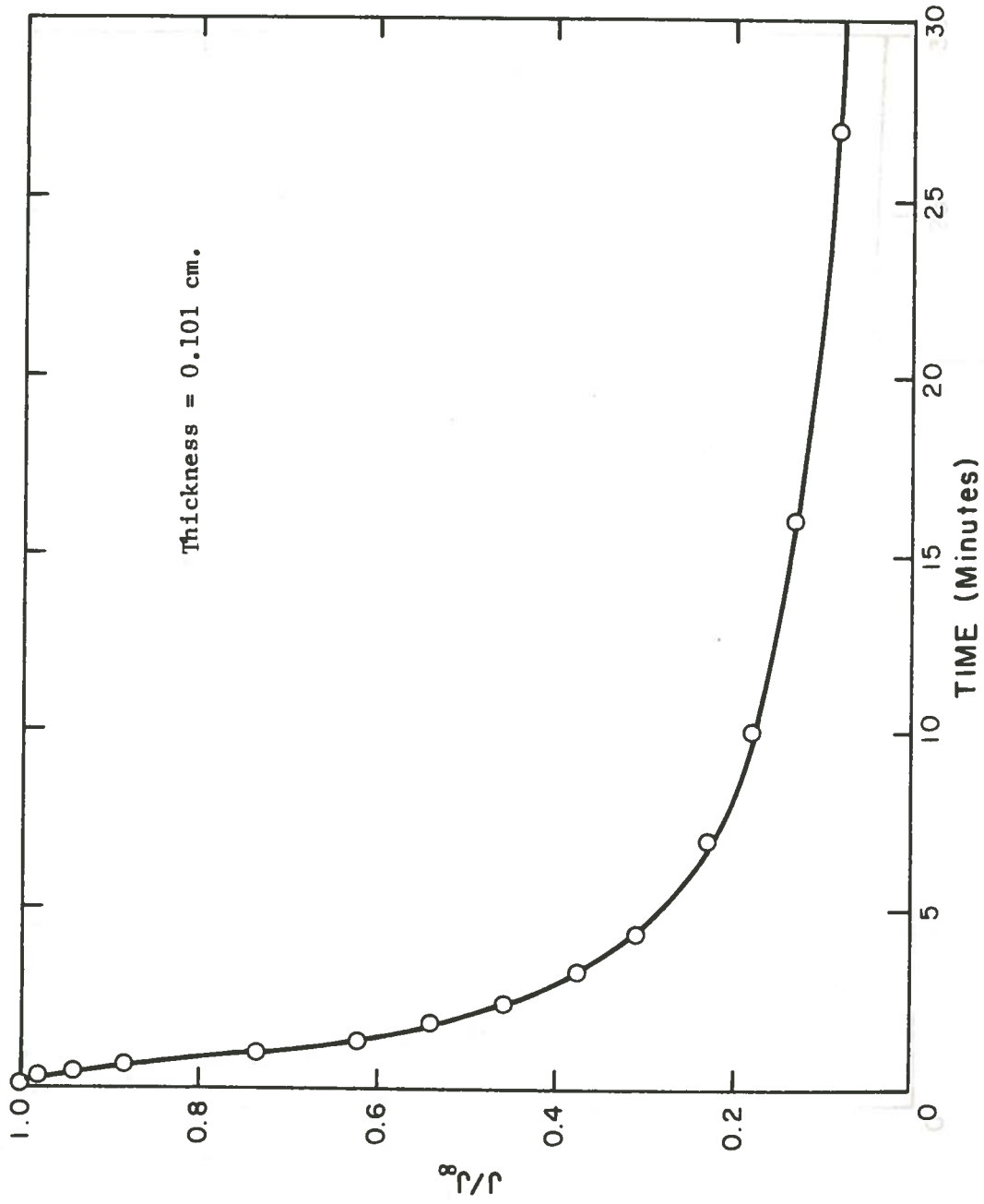


Figure 19. Normalized Output Flux of Hydrogen Versus Time for the Permeation Decay Transient of an Fe-0.013%S Alloy (Test No. 13-2).

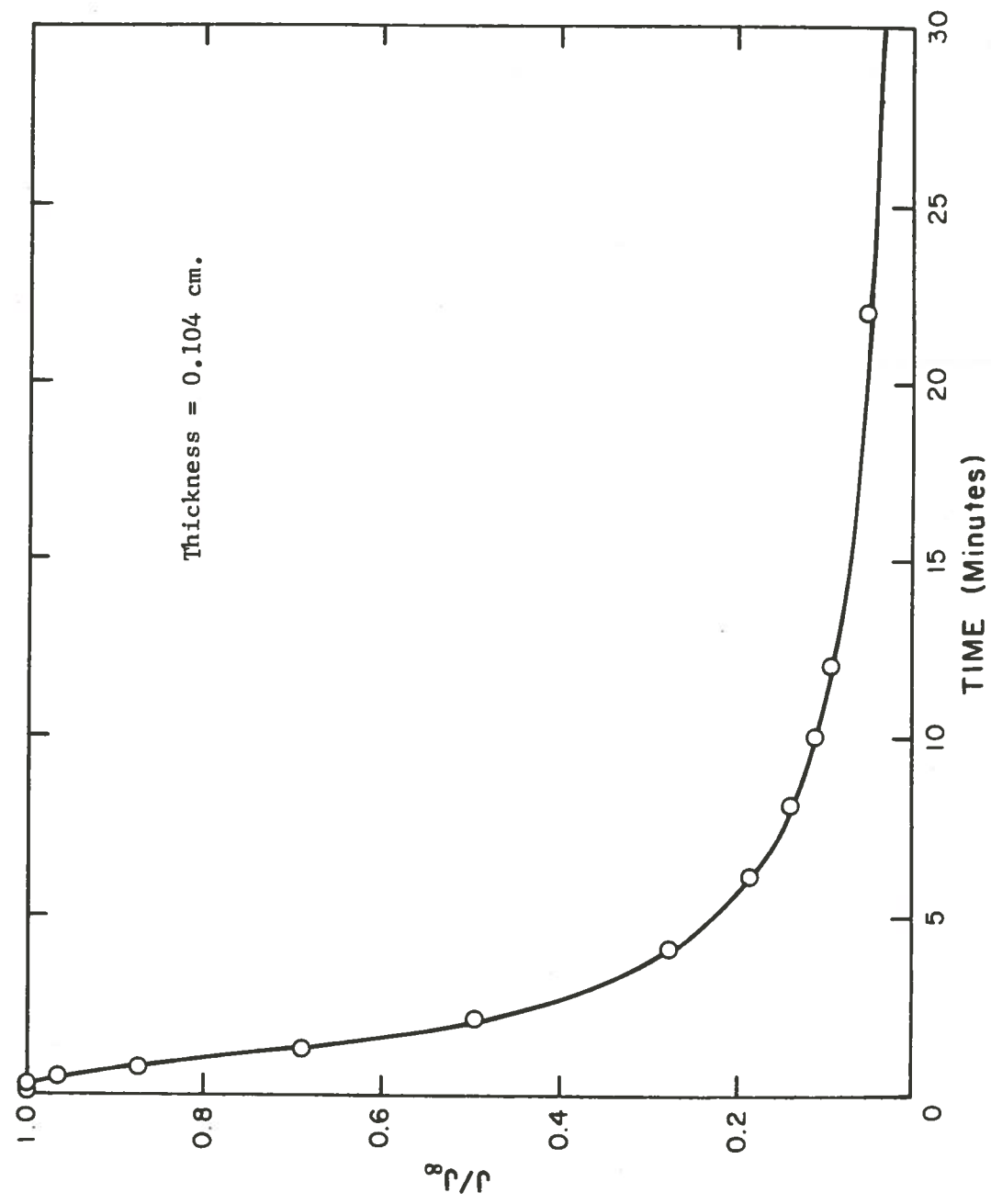


Table VII: Comparison of First Plarization Apparent Diffusion Coefficients with Values Obtained When Corrected for Relaxation Time.

| Alloy Type | Test No. | Relaxation Time | $D_{t_{lag}}$ (cm^2/sec) | | D_{t_b} (cm^2/sec) | |
|------------|----------|-----------------|--|-----------------------|--|-----------------------|
| | | | Measured | Corrected | Measured | Corrected |
| Fe-0.003%S | 3-1 | 15 sec | 3.28×10^{-6} | 3.44×10^{-6} | 3.02×10^{-6} | 3.38×10^{-6} |
| Fe-0.003%S | 3-2 | 15 sec | 2.92×10^{-6} | 3.01×10^{-6} | 1.82×10^{-6} | 1.91×10^{-6} |
| Fe-0.013%S | 13-1 | 12 sec | 4.80×10^{-6} | 4.97×10^{-6} | 3.38×10^{-6} | 3.60×10^{-6} |
| Fe-0.013%S | 13-2 | 17 sec | 6.53×10^{-6} | 6.96×10^{-6} | 4.71×10^{-6} | 5.32×10^{-6} |

Table VIII: Comparison of Second Polarization Apparent Diffusion Coefficients with Values Obtained When Corrected for Relaxation Time.

| Alloy Type | Test No. | Relaxation Time | $D_{t_{lag}}$ (cm^2/sec) | | D_{t_b} (cm^2/sec) | |
|------------|----------|-----------------|------------------------------|-----------------------|--------------------------|-----------------------|
| | | | Measured | Corrected | Measured | Corrected |
| Fe-0.003%S | 3-1 | 15 sec | 6.63×10^{-6} | 7.29×10^{-6} | 1.28×10^{-5} | 2.31×10^{-5} |
| Fe-0.003%S | 3-2 | 15 sec | 5.80×10^{-6} | 6.16×10^{-6} | 9.47×10^{-6} | 1.26×10^{-5} |
| Fe-0.013%S | 13-1 | 12 sec | 1.35×10^{-5} | 1.49×10^{-5} | 1.08×10^{-5} | 1.33×10^{-5} |
| Fe-0.013%S | 13-2 | 17 sec | 9.69×10^{-6} | 1.07×10^{-5} | 8.32×10^{-6} | 1.04×10^{-5} |

of reversible and irreversible hydrogen traps which alter the shape of the permeation rise transients.

4.3 Data Analysis

In order to compare the shape of permeation rise transients and thus the trapping characteristics of different alloys, the transients must be put into non-dimensional form. This has been shown [23,24] to be a useful technique for comparing the reversible trapping characteristics of different alloys. It is also quite useful for comparing them with the ideal diffusion behavior of hydrogen in iron. The normalized flux, J/J_{∞} is the same as was described previously; the normalized time is $\tau = Dt/a^2$, where D is the time-lag apparent diffusion coefficient for reversible trapping, t is the time measured from the start of polarization, and a is the membrane thickness.

4.3.1. Analysis of Irreversible Trapping

The normalized first and second permeation transients are shown in Figures 20 through 23 for all membranes which did not have their surfaces contaminated with corrosion products or show behavior indicative of short-circuit grain boundary diffusion. Once again, the figures indicate that irreversible trapping occurred in all membranes.

The quantity of irreversibly trapped hydrogen in each membrane was determined in the manner described in the Permeation Results section. This is only an estimate of the amount of irreversibly trapped hydrogen since slight variations in the

Figure 20. Normalized Permeation Transients for Fe-0.003%S Alloy (Test No. 3-1).

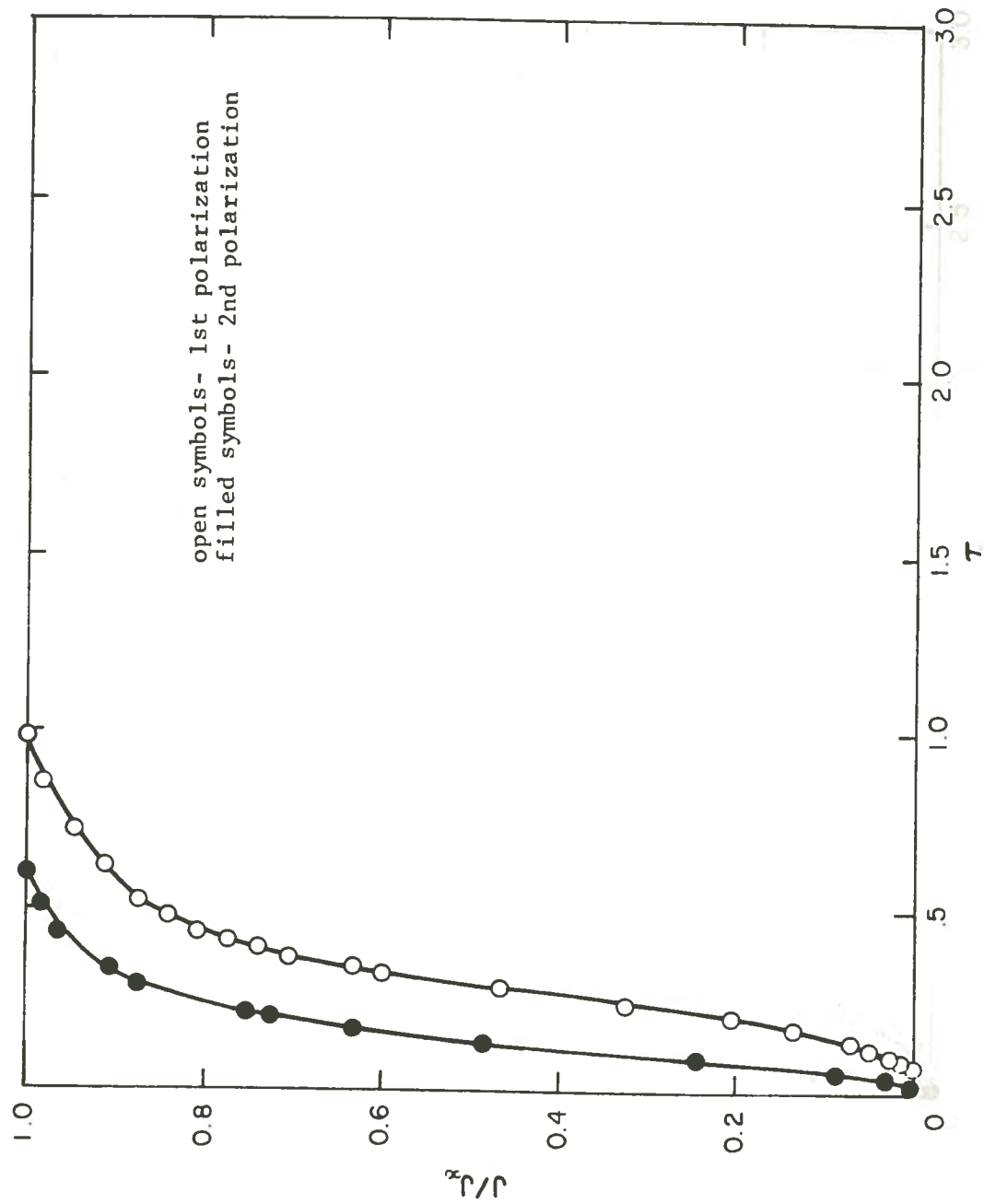


Figure 21. Normalized Permeation Transients for Fe-0.003%S Alloy (Test No. 3-2).

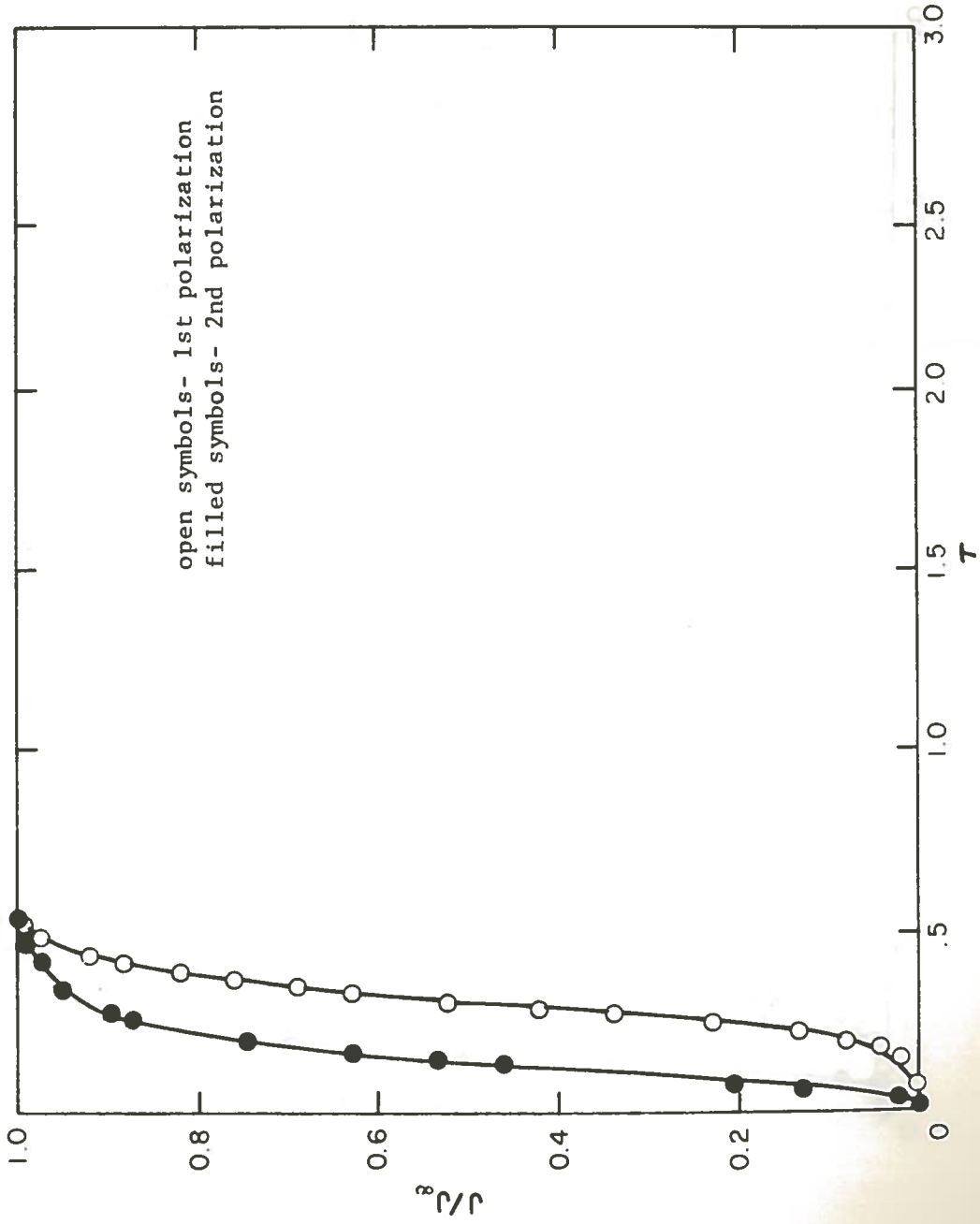


Figure 22. Normalized Permeation Transients for Fe-0.013%S Alloy (Test No. 13-1).

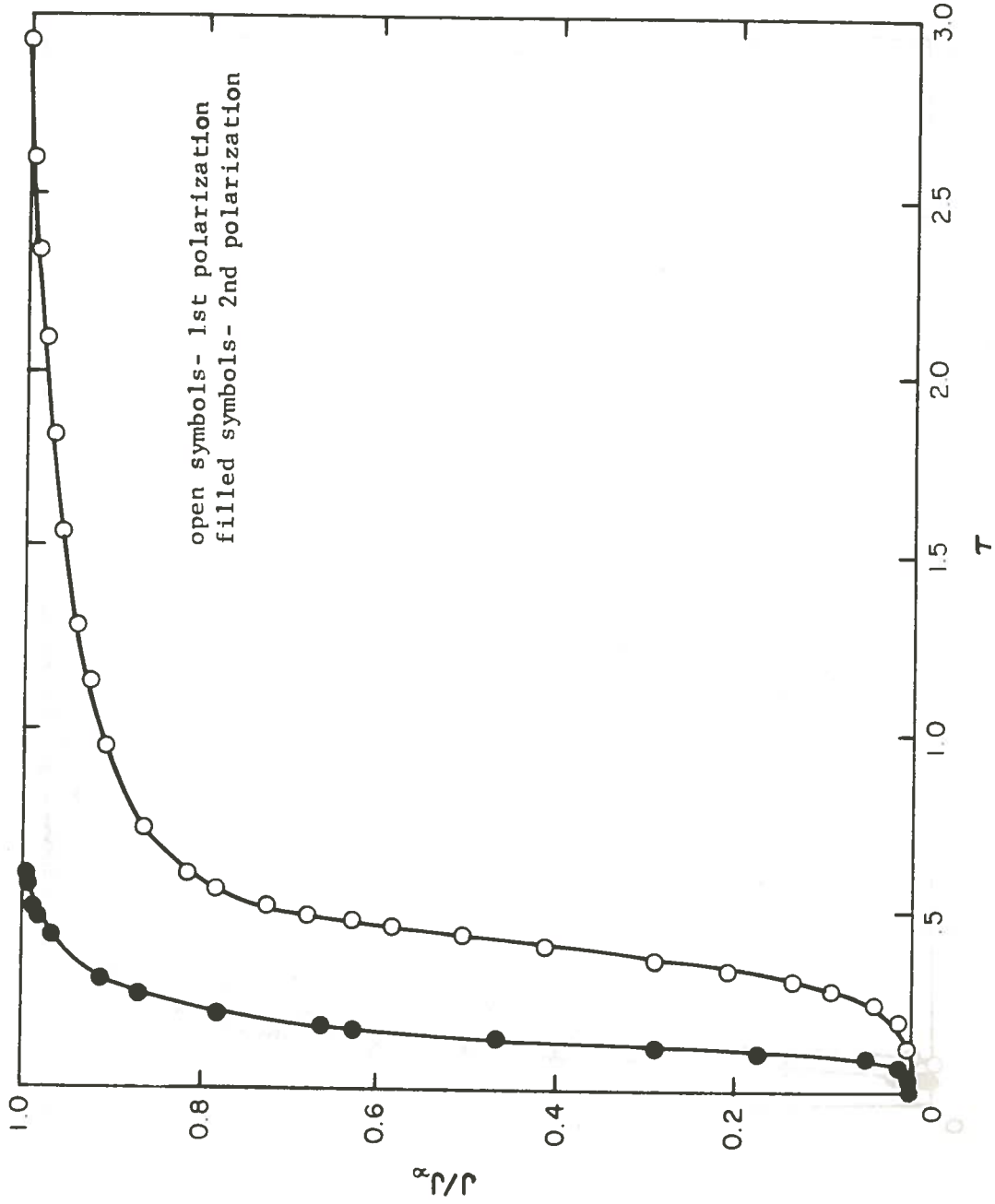
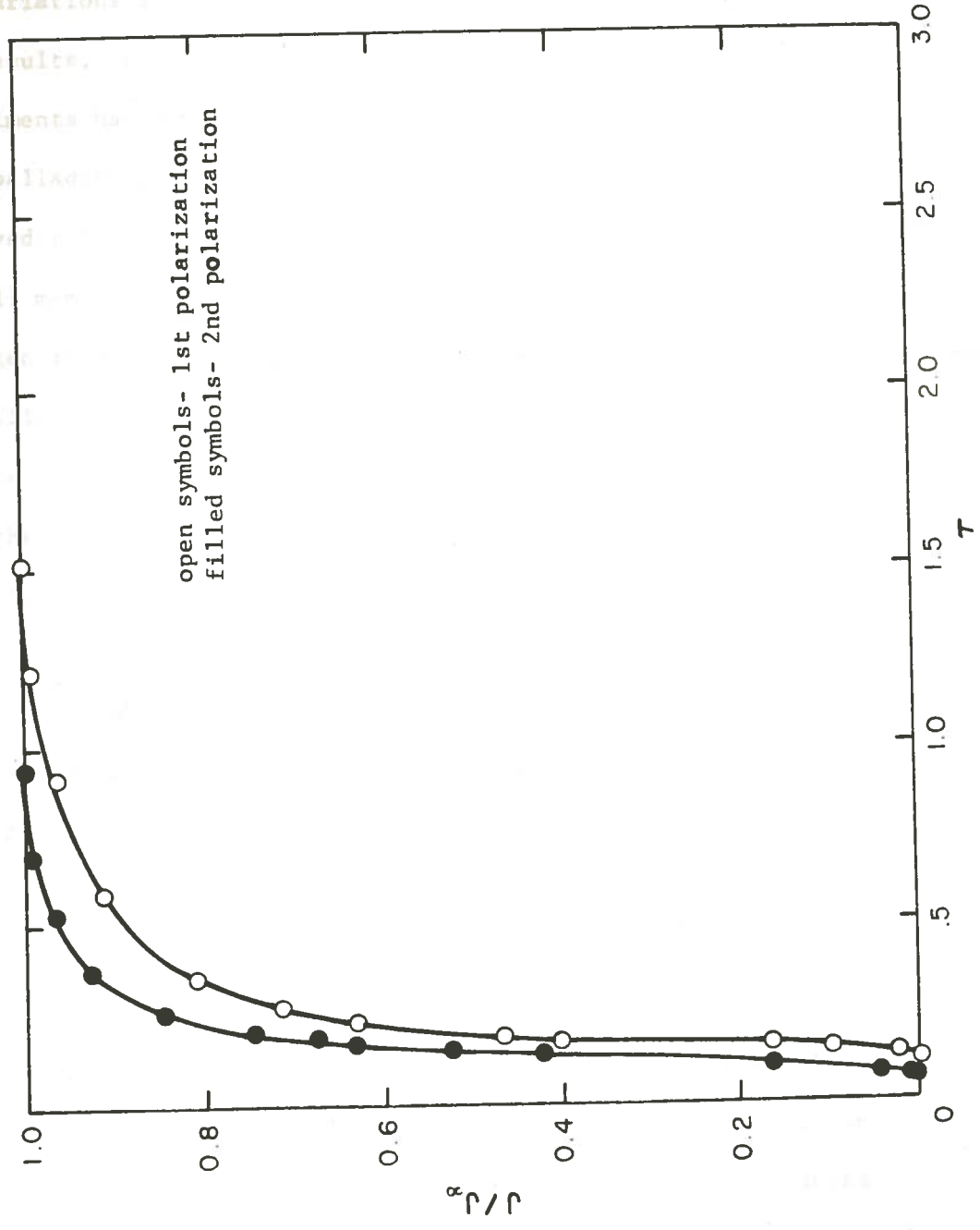


Figure 23. Normalized Permeation Transients for Fe-0.013%S Alloy (Test No. 13-2).

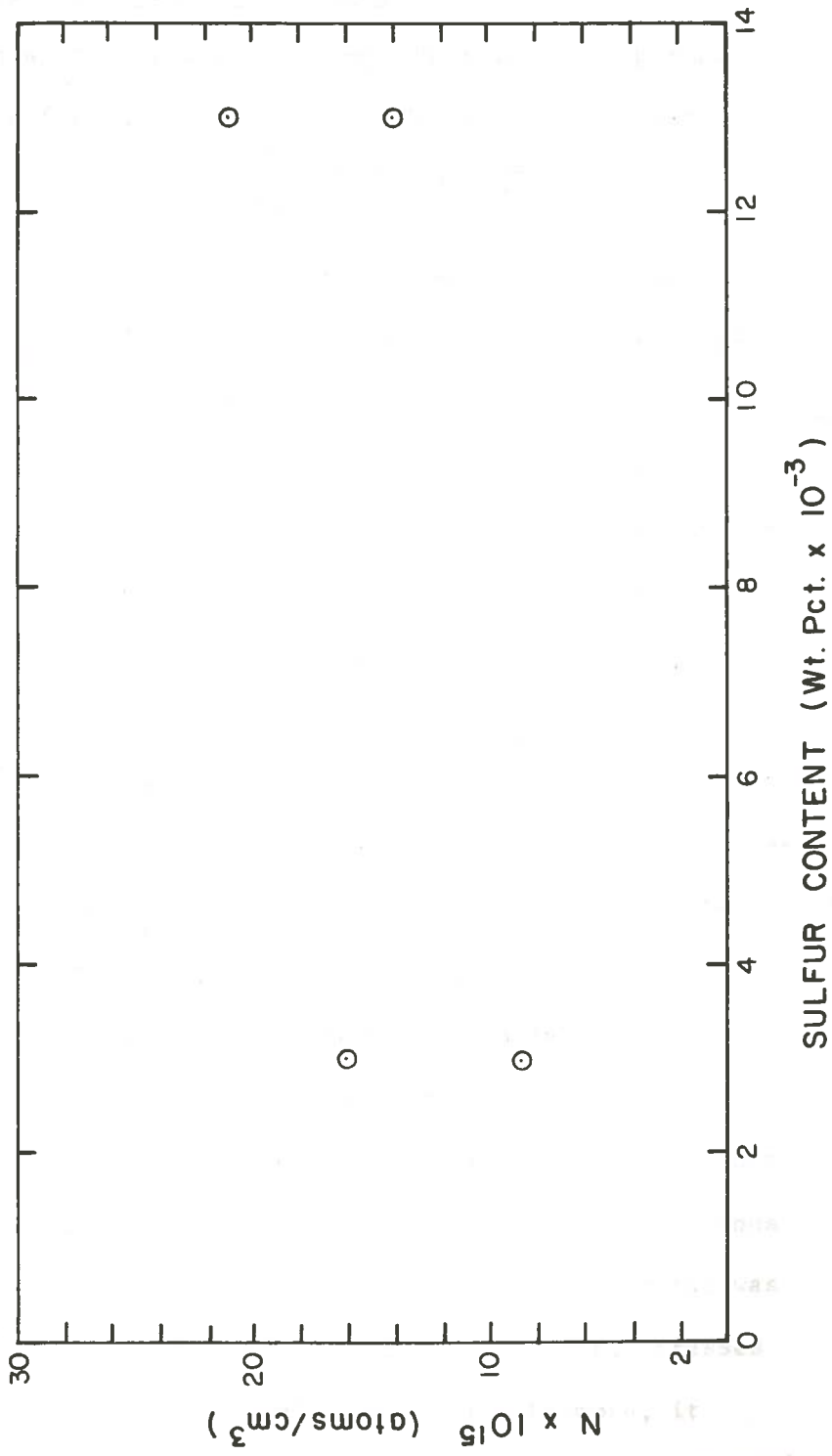


hydrogen entry conditions between successive polarizations and variations in the steady-state hydrogen flux can affect the results. However, all membranes used in the permeation experiments had similar mirror-like polished surfaces and were palladium plated in a similar manner; therefore, it is believed that similar hydrogen entry conditions were obtained for all membranes and that the quantity of irreversibly trapped hydrogen in the metal membranes can be compared quantitatively for different alloy compositions. In addition to similar surface preparation, microstructural analysis has revealed that the only differences in the two alloys were the sulfide inclusion content and a small difference in the average grain size.

Of the two alloys, the Fe-0.003%S alloys had the smallest grain size and thus the largest surface (grain boundary surface area) to volume ratio. If grain boundaries were acting as irreversible hydrogen traps, the Fe-0.003%S alloy would contain many more irreversible traps than the Fe-0.013%S alloy and would be expected to trap a greater quantity of hydrogen.

For each permeation membrane the quantity of irreversibly trapped hydrogen per unit volume of permeation membrane is shown in Figure 24 as a function of alloy sulfur content. The results show that the alloy with higher sulfur content irreversibly trapped the greater quantity of hydrogen. The results also rule out grain boundary trapping as the major source of irreversible hydrogen

Figure 24. Quantity of Irreversibly Trapped Hydrogen as a Function of Alloy Sulfur Content.



trapping because the grain size trend is in the wrong direction.

4.3.2. Analysis of Reversible Trapping

Based on simple diffusion theory the normalized permeation rise transient for the diffusion of hydrogen is described by:

$$J/J_{\infty} = 1 + 2 \sum_{n=1}^{\infty} (-1)^n \exp(-n^2 \pi^2 \tau) \quad 4.3$$

for boundary condition similar to those used in the permeation experiments, where J/J_{∞} is the normalized hydrogen flux, and τ is the normalized time. This equation was solved by digital computer for various values of τ and the computed results are shown in Figure 25 with a smooth curve drawn between them. Since trapping is not taken into account by simple diffusion theory this curve represents the shape of the rise transient in the absence of trapping.

Typical permeation transients for the second polarization of Fe-0.003%S and Fe-0.013%S alloy membranes are shown in Figure 26 in normalized form and are compared to the permeation transient obtained from simple diffusion theory. The shape of the permeation rise transients for each alloy is essentially the same as the rise transient obtained from simple diffusion theory. This indicates that the FeS inclusions in the membranes do not act as reversible hydrogen traps under the charging conditions of the permeation tests. It also indicates that the metal was in the fully annealed condition and that no residual stresses were present to act as reversible traps. Furthermore, it indicates that solid-solution sulfur in iron does not reversibly

Figure 25. Normalized Permeation Rise Transient as Predicted by Simple Diffusion Theory.

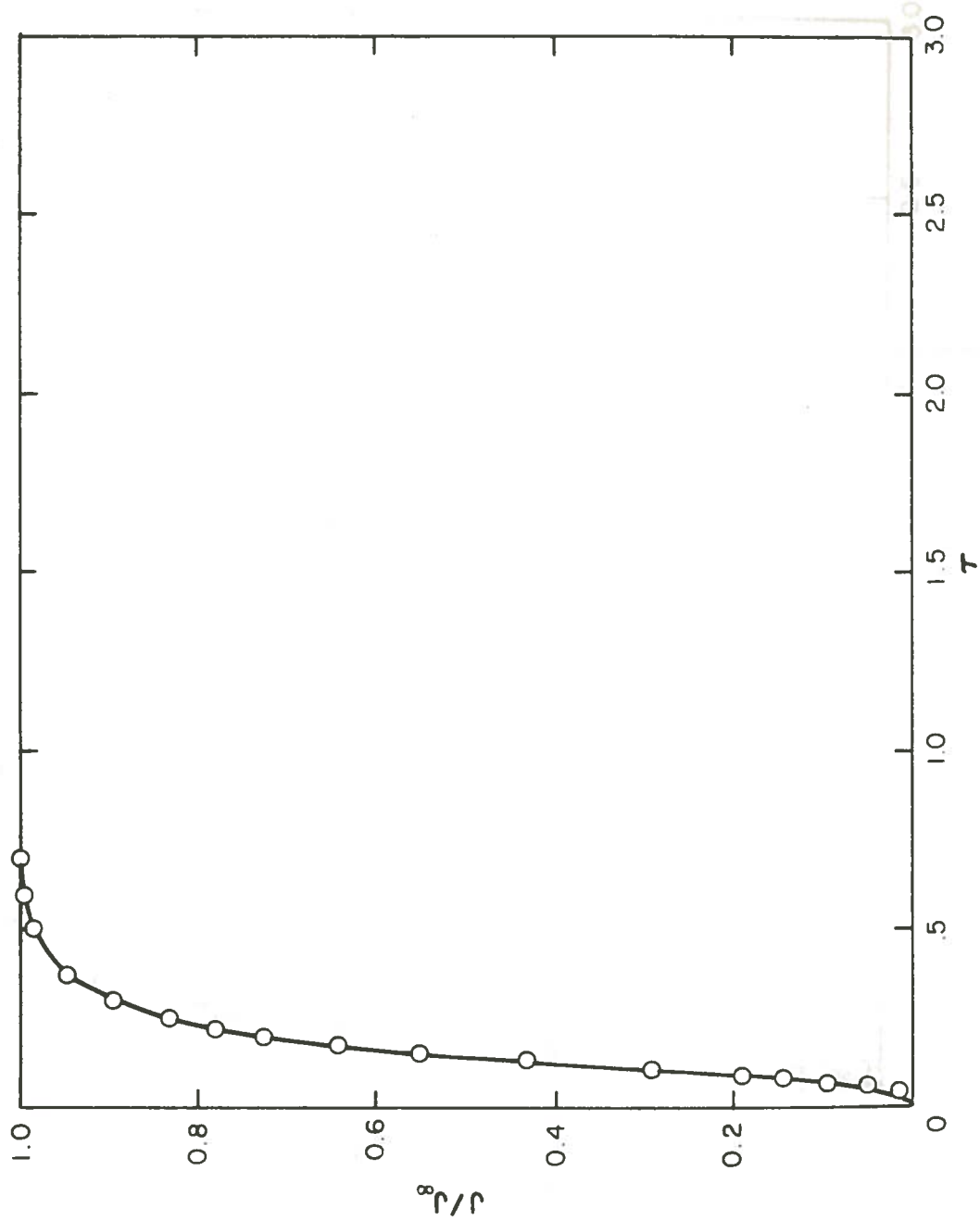
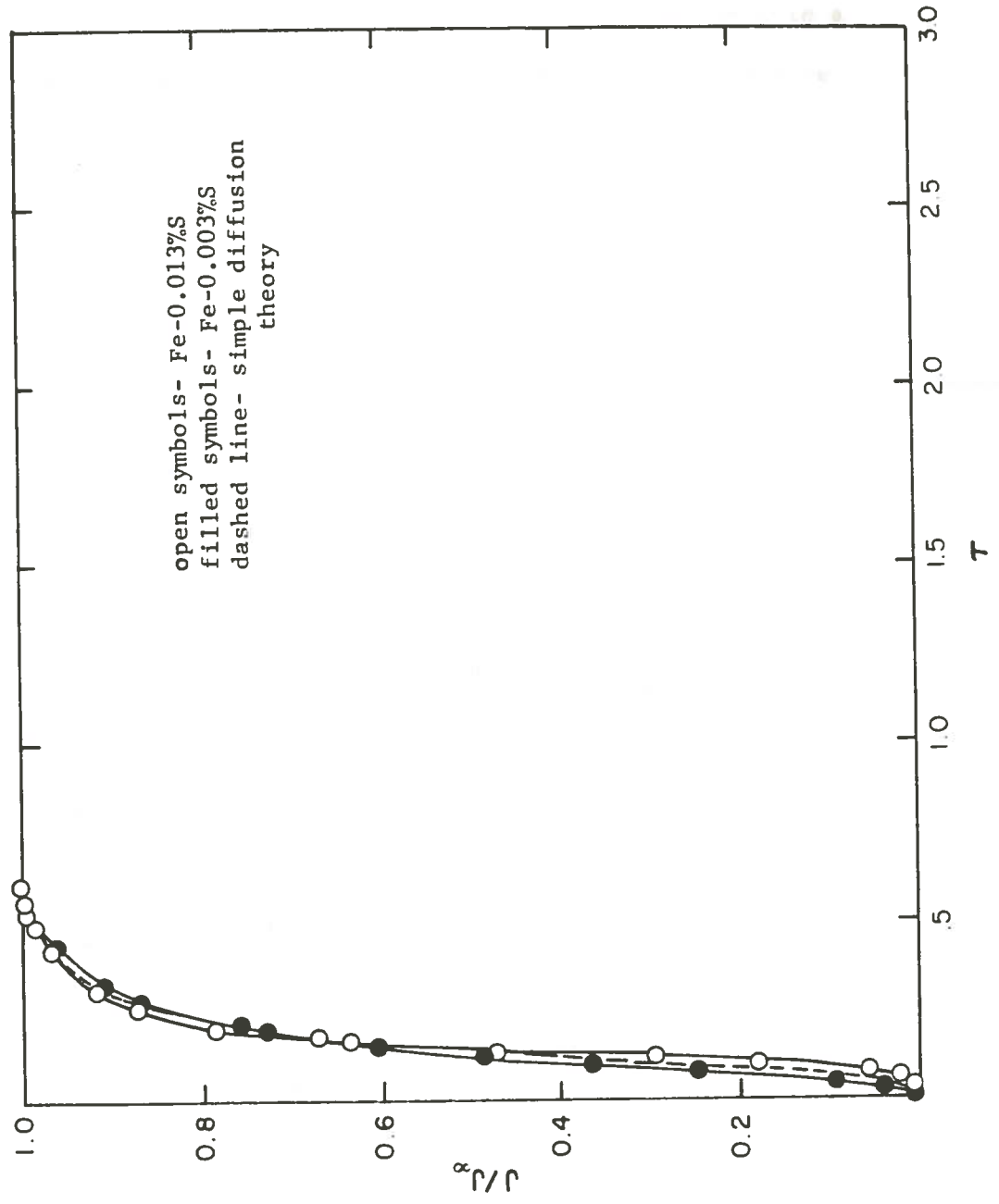


Figure 26. Normalized Permeation Rise Transients for the Second Polarization of Fe-S Alloys Compared With That of Simple Diffusion Theory.



trap hydrogen in measurable quantities because, as discussed previously, reversible trapping of hydrogen will result in a permeation transient which lies below that of ideal lattice diffusion on the normalized time-flux axes.

4.4 Summary

The results of room temperature electrochemical permeation experiments on fully annealed iron-sulfur alloys have shown that irreversible hydrogen traps were present in all permeation membranes. The quantity of irreversibly trapped hydrogen in each membrane was estimated and the results indicate that the quantity of irreversibly trapped hydrogen in iron increases with increasing sulfur content. Also, comparison of the normalized second polarization transients with that of simple diffusion theory has shown that neither iron-sulfide inclusions nor solid-solution sulfur in iron behave as reversible hydrogen traps.

CHAPTER V
CONCLUSIONS

The achieved goal of this study was to use the electrochemical permeation technique to study the effect of the impurity element, sulfur, on the diffusion and trapping behavior of hydrogen in iron. Polycrystalline iron alloys with sulfur contents ranging from 0.003 wt. pct. to 0.013 wt. pct. were alternately cold-rolled and annealed to obtain microstructurally similar permeation membranes approximately 1 mm in thickness.

All membranes were charged with hydrogen using a cathodic current density of 0.8mA/cm^2 . Comparison of the first and second polarization transients of the alloys revealed that iron-sulfide inclusions behave as irreversible hydrogen traps. Also, it was found that neither iron-sulfide inclusions nor solid-solution sulfur in iron behave as reversible hydrogen traps to any measurable degree.

BIBLIOGRAPHY

16. R. A. Ori...
p. 883
17. R. A. Ori...
p. 10
1. T. Asaoka, Thèse Docteur-Ingenieur, University of Paris-Sudan, 1976.
2. J. P. Laurent, G. Lapasset, M. Aucouturier, and P. Lacombe, Hydrogen in Metals, ed. by I. M. Bernstein and A. W. Thompson, ASM, Ohio, p. 559, 1974.
20. N. J. ...
3. A. H. Kumnick and H. H. Johnson, *Met. Trans.*, vol. 5, p. 1200, 1974.
21. R. M. ...
4. G. M. Evans and E. C. Rollason, *Journal of the Iron and Steel Institute*, vol. 207, p. 1591, 1969.
22. M. ...
5. D. M. Allen-Booth and J. Hewitt, *Acta Met.*, vol. 22, p. 171, 1974.
23. A. ...
6. G. M. Pressouyre, PhD Thesis, Carnegie-Mellon University, 1977.
24. G. K. ...
7. T. Boniszewski, Report P/10/66 of the British Welding Research Association, London, 1966.
25. G. D. ...
8. G. M. Pressouyre, *Acta Met.*, vol. 28, p. 895, 1980.
26. G. M. ...
9. M. Iino, *Met. Trans.*, vol. 10A, p. 1691, 1979.
27. S. M. ...
10. A. R. Troiano, *ASM Trans.*, vol. 52, p. 54, 1960.
211. L. S. Darken and R. P. Smith, *Corrosion*, vol. 5, p. 1, 1949.
12. G. M. Pressouyre and I. M. Berstein, *Met. Trans.*, vol. 9A, p. 1571, 1973.
29. G. ...
13. C. A. Zapffe and C. E. Sims, *Metals and Alloys*, vol. 11, p. 145, 1940.
30. M. ...
14. M. G. Fontana and N. D. Greene, Corrosion Engineering, McGraw-Hill, eds., 2nd edit., pp. 109-115, 1967.
31. A.S.M. ...
15. G. G. Hancock and H. H. Johnson, *Trans. AIME*, vol. 236, p. 513, 1966.
32. C. ...
33. American ...
book of ...

16. R. A. Oriani, Ber. der. Bunsen-Gesellschaft, vol. 76, p. 848, 1972.
17. R. A. Oriani and P. H. Josephic, Acta Met., vol 22, p. 1065, 1974.
18. R. A. Oriani and P. H. Josephic, Acta Met., vol. 25, p. 979, 1977.
19. E. Lunarska, A. Zielinski and M. Smialowski, Acta Met., vol. 23, p. 305, 1977.
20. N. J. Petch and P. Stables, Nature, vol. 169, p. 842, 1952.
21. R. M. Barrer, Trans. Faraday Soc., vol. 35, p. 628, 1939.
22. M. A. V. Devanathan and Z. O. J. Stachurski, Proc. Roy. Soc., vol. A270, p. 90, 1962.
23. A. McNabb and P. K. Foster, Trans AIME, vol. 227, p. 628, 1963.
24. G. R. Caskey, Jr. and W. L. Pillinger, Met. Trans., vol. 6A, p. 467, 1975.
25. O. D. Gonzalez, Trans. AIME, vol. 245, p. 607, 1969.
26. G. M. Pressouyre, Met. Trans., vol. 10A, p. 1571, 1979.
27. S. Marich and R. Player, Met. Trans., vol. 1, p. 1853, 1970.
28. J. F. Elliott, M. Gleiser and V. Ramakrishna, Thermochemistry for Steelmaking, Addison-Wesley, eds., Redding Mass., 1963.
29. G. K. Sigworth and J. F. Elliott, Metal Science, vol. 8, p. 298, 1974.
30. M. Weinstein and J. F. Elliott, Trans. AIME, vol. 227, p. 382, 1963.
31. A.S.M. Metals Handbook, vol. 8, 8th Ed., 1973.
32. C. E. Sims, Trans. AIME, vol. 215, p. 367, 1959.
33. American Society for Testing and Materials, 1975 Annual Book of ASTM Standards, Easton, Md.

34. J. E. Hilliard, Quantitative Microscopy, ed. by R. T. DeHoff and F. N. Rhines, McGraw-Hill Book Co., N.Y., p. 45, 1968.
35. E. E. Underwood, Quantitative Microscopy, ed. by R. T. DeHoff and F. N. Rhines, McGraw-Hill Book Co., N.Y., p. 77, 1968.
36. P. Fischer and J. Jankowski, Naval Air Development Center Report No. NADC-72045-VT, 12 May 1972.
37. R. N. Rhoda, Trans. Inst. Metal Finishing, vol. 36, p. 82, 1959.

VITA

Dale A. Jones was born in Lake Charles, Louisiana on May 4, 1957, the son of Eleanor E. Jones and Martin V. Jones. After graduating from Lake Charles High School in 1975, he entered Louisiana State University at Baton Rouge in August, 1975. He received a Bachelor of Science degree in Mechanical Engineering from that institution in December, 1980. In January, 1981, he returned to Louisiana State University and is currently completing work toward a Master of Science degree in Mechanical Engineering.

Permanent Address: 2005 Ernest Street
Lake Charles, Louisiana 70601